Theory of quantum transport in three-dimensional Weyl electron systems

PhD Thesis

Theory of quantum transport in three-dimensional Weyl electron systems

（３次元ワイル電子系における電子輸送の理論）

Yuya Ominato

Department of Physics, Graduate School of Science
Tohoku University

2015

Contents

Abstract

Recently, many researchers are attracted by a new type of systems where the conduction band and the valence band stick together at a certain point in the Brillouin zone. Such kinds of 3D gapless systems are called Dirac semimetals or Weyl semimetals. Weyl semimetal has more than two band-touching points (Weyl points), the electronic structure around the band-touching points is described by 2×2 Weyl Hamiltonian. In the Dirac semimetal, on the other hand, a pair of the Weyl-point happen to merge at a single momentum, around which the electronic states are described by 4×4 Dirac Hamiltonian. It is known that Dirac semimetal emerges when a system has both the spacial-inversion (I) symmetry and the time-reversal (T) symmetry, and the Weyl semimetals is obtained by breaking either of I and T symmetry. Emergence of the Weyl semimetal phase by breaking I symmetry was discussed in the research on phase transition of topological insulator, and the weyl semimetal by breaking T symmetry was also discussed in iridium oxide materials. The Weyl semimetal phase by breaking T symmetry was also discussed in a relatively simple model which is composed of a superlattice structure of topological insulator and normal insulator. Motivated by these theoretical proposals, the enormous experimental effort has been put in searching for candidate materials. The Dirac semimetal phase was recently found in Cd_3As_2 and $NaBi_3$ and Weyl semimetal was in TaAs, NbP and TaP.

One of important features of Weyl semimetal is existence of topological surface states. The Weyl semimetal can be regarded as a collection of topological / trivial 2D systems on xy-plane parameterized by the momentum p_z. In this particular case, the energy gap is closed at certain momenta $p_z = \pm p_0$ and the system is the quantum Hall insulator in the region of $-p_0 < p_z < p_0$ while normal trivial insulator outside. Since the edge states appear only in the quantum Hall phase, the left and right edge (surface) state bands emerge in $-p_0 < p_z < p_0$ so as to connect a pair of bulk linear bands around the point nodes. Consequently, the equi-energy line of the surface band does not close in itself but bridges the two bulk bands. This is called Fermi arc. The Fermi arc was directly observed by the angle resolved photo emission spectroscopy in various materials.

Quantum transport in single-node Weyl electron

We studied the electronic transport in single-node disordered Weyl electron systems. At the Weyl point, the Fermi surface becomes a point, so that the semiclassical Boltzmann transport theory fails and we have to incorporate the level broadening effect appropriately. We use a self-consistent Born approximation which is one of the theoretical methods to treat the level broadening effect. In the Weyl electron system, specific form of the impurity

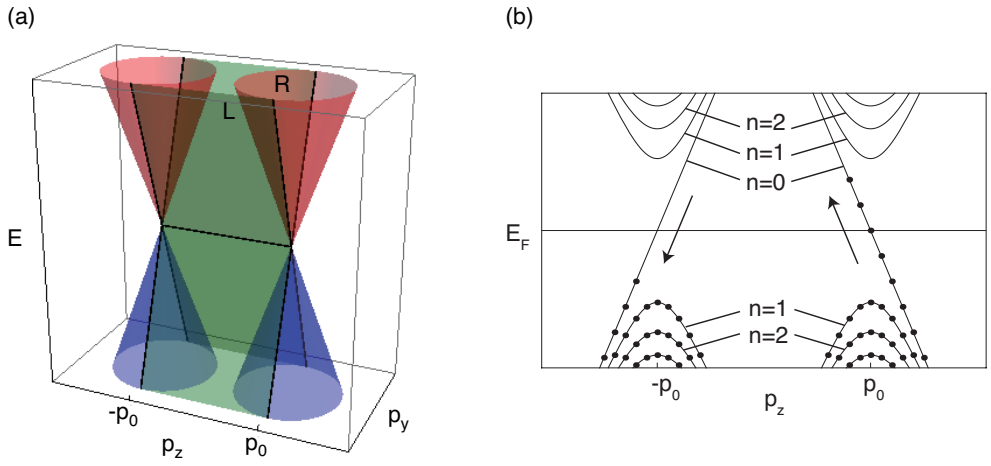

Figure 1: (a) Schematic energy band structure of the Weyl semimetal. There is a pair of band touching points (Weyl points) at $p_z = \pm p_0$. Fermi arc connect the Weyl points. (b) Schematic energy spectrum in the presence of the magnetic field.

potential crucially affect the behavior of the conductivity, so that we considered two types of the long-range potentials, the Gaussian and Coulomb potential. In the Gaussian case, we found that there is a critical disorder strength, and the behavior is significantly different between the weak disorder regime and the strong disorder regime. At the Weyl point, the conductivity vanishes in the weak disorder, but the conductivity has a finite value and increases with the increase of disorder strength in the strong disorder. In a finite Fermi energy, the conductivity is well approximated by the Boltzmann conductivity and exhibits usual metallic behavior, but once the level broadening exceeds the Fermi energy the conductivity exhibits unusual metallic behavior and increases with the increase of disorder strength. In the Coulomb case, on the other hand, there is no critical behavior, and the minimum conductivity is almost independent of the effective fine structure constant which characterize the disorder strength. We discussed a condition for the existence of the critical behavior, and found that the certain criteria for the existence of the critical behavior for a general screened impurity potential.

Magnetotransport in the Weyl semimetal

We studied the magneto-transport in a Weyl semimetal. In the presence of the magnetic field, the linear energy band is quantized into the Landau levels dispersing to the direction parallel to the magnetic field. One of the characteristic feature of the Weyl semimetal is the existence of the chiral 0th Landau level. Applying the electric field parallel to the magnetic field, we observe negative magneto-resistance which is related to the chiral anomaly. This is because each 0th mode is relaxed only by the inter-valley scattering which is suppressed for a smooth potential. Here, we calculated the magneto conductivity of the Weyl semimetal with and without surface-boundary. The conductivity without surface is independent of the magnetic field. The conductivity increases exponentially with the

increase of potential range. This is because the inter-valley scattering rate is exponentially small. The conductivity with surface, on the other hand, is proportional to the magnetic field in a super-linear manner and increases in a power function of the potential range. This difference comes from the contribution of the surface states. In condition that the potential-range is sufficiently large to prohibit the inter-valley scattering, there is a scattering process through the surface states. As a result, the conductivity increases rather like a exponential function than a power function as a function of the potential range.

Chapter 1

Introduction

In this chapter, we explain the electronic structure of Dirac semimetals and Weyl semimetals. They are three-dimensional (3D) gapless systems and exhibit various unusual physical properties not observed in conventional systems. In this thesis, we study the electronic transport properties in these 3D gapless systems.

1.1 3D gapless systems – Dirac semimetals and Weyl semimetals

In recent condensed-matter physics, many researchers are attracted by a new type of systems where the conduction band and the valence band stick together at a certain point in the Brillouin zone. One of the famous examples is graphene which has the 2D gapless electronic structure and exhibits many characteristic physical properties. In addition to the 2D gapless systems, the electronic properties of the 3D gapless systems is also one of great interests. Such kinds of 3D gapless systems are called Dirac semimetals or Weyl semimetals. [1, 2, 3, 4, 5, 6, 7, 8, 9, 10, 11, 12, 13] Weyl semimetal has more than two band-touching points (Weyl points), and the electronic structure around the band-touching points is described by 2×2 Weyl Hamiltonian. In the Dirac semimetal, on the other hand, a pair of the Weyl-point happen to merge at a single momentum, around which the electronic states are described by 4×4 Dirac Hamiltonian. Fig. 1.1 shows the schematic energy dispersion of the Weyl semimetal, where the conduction and valence bands are touching at $p_z = \pm p_0$. It is known that Dirac semimetal emerges when a system has both the spacial-inversion (I) symmetry and the time-reversal (T) symmetry, and the Weyl semimetal is obtained by breaking either of I and T symmetry. Emergence of the Weyl semimetal phase by breaking I symmetry was discussed in the research on phase transition of topological insulator, [14] and the Weyl semimetal by breaking T symmetry was discussed in iridium oxide materials. [3] The Weyl semimetal phase by breaking T symmetry was also discussed in a relatively simple model which is composed of a superlattice structure of topological insulator and normal insulator. [1] Motivated by these theoretical proposals, the enormous experimental effort has been put in searching for candidate materials. The Dirac semimetal phase was recently found in Cd_3As_2 and $NaBi_3$ [15, 16, 17] and Weyl semimetal was in TaAs, NbP and TaP. [18, 19, 20, 21] The lattice structure of Cd_3As_2 and TaAs are depicted in Fig. 1.2

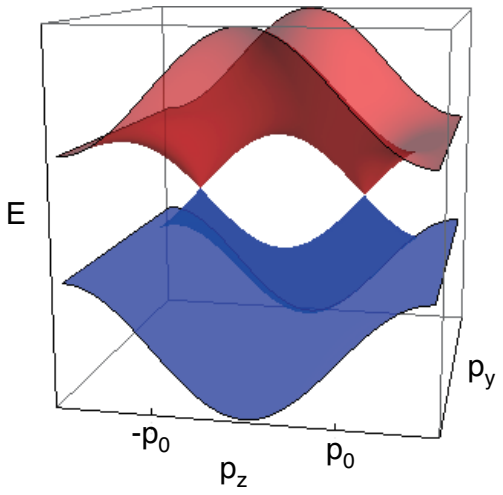

Figure 1.1: Schematic energy band structure of the Weyl semimetal. There is a pair of band touching points (Weyl points) at $p_z = \pm p_0$.

and 1.3. The bulk linear band structure is observed by the angle resolved photoemission spectroscopy (ARPES), and the ARPES data is shown in Fig. 1.2 and 1.3.

One of important features of Weyl semimetals is existence of topological surface states. Fig. 1.4 shows schematic energy spectrum of surface states. [19] The Weyl semimetal can be regarded as a collection of topological / trivial 2D systems on xy-plane parameterized by the momentum p_z. In this particular case, the energy gap is closed at the momenta $p_z = \pm p_0$ and the system is the quantum Hall insulator in the region of $-p_0 < p_z < p_0$ while normal trivial insulator outside. Since the edge states appear in the quantum Hall phase, the left and right edge (surface) state bands emerge in $-p_0 < p_z < p_0$ so as to connect a pair of bulk linear bands around the point nodes as shown in Fig. 1.4. Consequently, the equi-energy line of the surface band does not close in itself but bridges the two bulk bands. This is called Fermi arc. The Fermi arc was directly observed by the ARPES in various materials as shown in Fig. 1.3, and this is a strong evidence for the Weyl semimetal.

1.2 Transport properties in 3D Weyl systems

Motivated by the experimental discovery of the Dirac semimetals and the Weyl semimetals, many researchers are studying the physical properties of these 3D gapless systems in the theoretical and experimental points of view. Various unusual properties are reported, but there are many interesting unresolved problems.

In this thesis, we study the electronic transport properties in the 3D Weyl electron systems. The theme is categorized into two parts, quantum transport in 3D Weyl electrons and magnetotransport in the Weyl semimetal. In the following subsections, the background of the two problems are explained in succession.

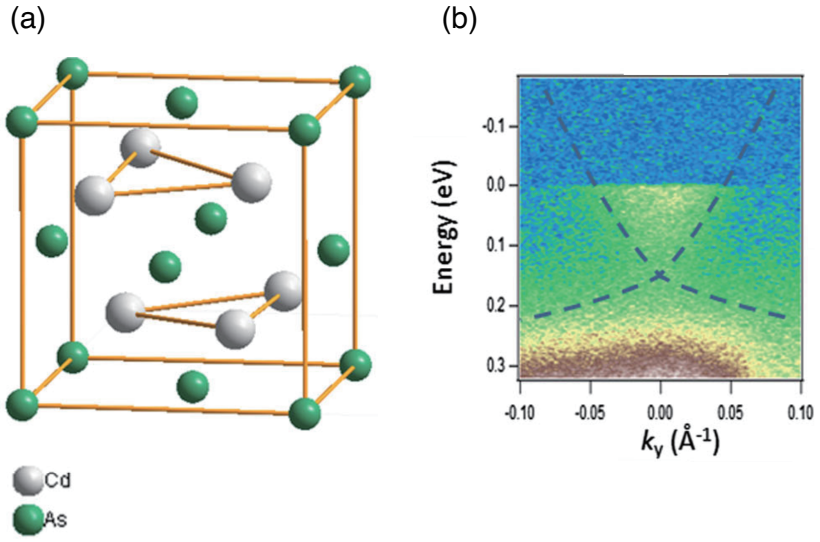

Figure 1.2: The panels (a) and (b) show the lattice structure of Cd_3As_2 and the experimentally observed band structure by ARPES, respectively. The black dashed lines represent the bulk gapless band structure and it is observed. [15]

1.2.1 Quantum transport in Weyl electrons

The transport property of the point-node gapless system is significantly different from the conventional systems. When the Fermi energy is right at the Weyl point, in particular, it is highly nontrivial if the system is metallic or insulating because the electronic density of states is tiny at the point node. The conventional Boltzmann transport theory assumes the Fermi energy is much greater than the inverse scattering time so that the Fermi surface is well defined. This assumption does not apply to the point node case, because the Fermi energy is zero and the Fermi surface becomes a point. To treat this situation, we need some improved theoretical approach which appropriately incorporates the finite level broadening effect.

Historically, the electronic transport in a gapless system was examined for 2D Weyl Hamiltonian in research on graphene using various theoretical methods, [22, 23, 24, 25, 26, 27, 28, 29, 30] for example, a self-consistent Born approximation (SCBA) which properly treat the finite level broadening effect, and the finite-size Kubo formula method established for diffusive metallic systems. They are applicable to both zero and finite Fermi energy. Using these theoretical methods, the characteristic transport properties in 2D Weyl were clarified. One of the important results is that the transport properties in 2D Weyl strongly depend on the type of scattering potential. In the conventional metals, the detailed feature of the scatterer does not matter in the qualitative transport property and therefore the theoretical calculation typically assumes the simplest scattering potential such as the short-range or white-noise potential which is represented by a delta function. In 2D Weyl system, however, the Fermi energy dependence of the conductivity and the numerical factor in the minimum conductivity (conductivity at the Weyl point) were found to be quite

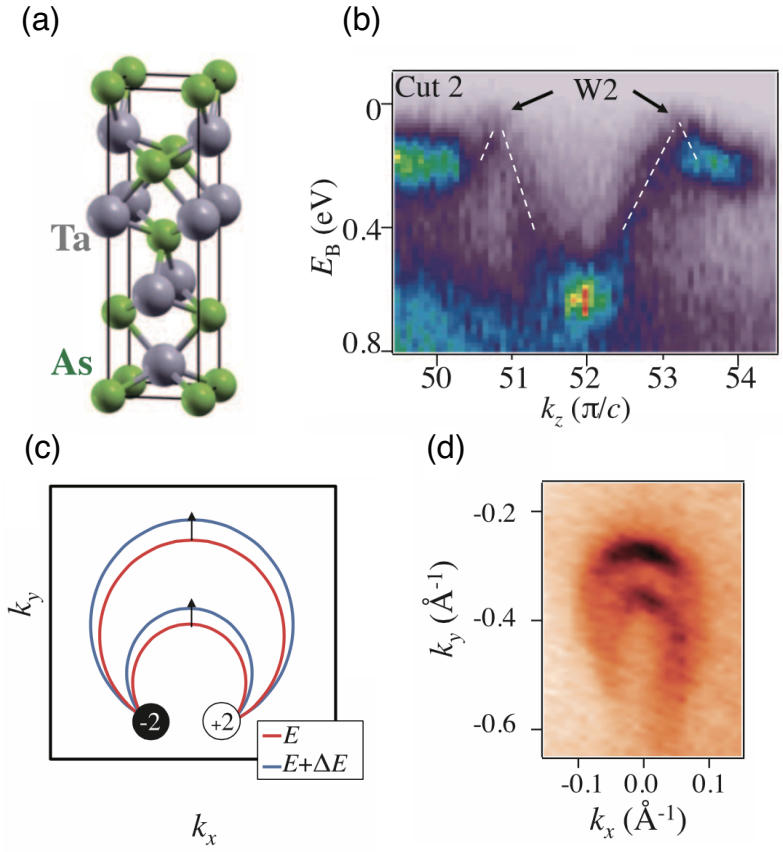

Figure 1.3: (a) The lattice structure of TaAs. (b) The experimentally observed band structure by ARPES. W2 represents the Weyl points and the white dashed lines represent the observed gapless linear band structure. (c) The schematic showing the evolution of the Fermi arcs. The black and white circles represent the Weyl points and the blue and red curves represent the Fermi arcs. (d) The experimentally observed Fermi arcs. The Fermi arcs are directly observed by ARPES. [18]

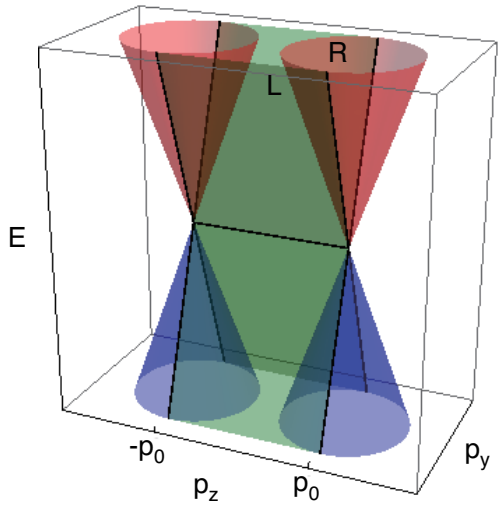

Figure 1.4: Schematic energy spectrum of Fermi arc. There are two linear bands which bridge the two bulk Weyl cones, and it disperses only in p_y-direction.

different between various types of scatterers. Therefore, the consideration of the detailed scattering potential is crucial in arguing about the transport property in the Weyl system. Fig. 1.5 shows examples of the numerically calculated conductivity. In the energy region away from the Weyl point, the conductivity is almost independent of the Fermi energy in the short-range potential case, while the conductivity is proportional to $\varepsilon_{\rm F}^2$ ($\varepsilon_{\rm F}$: the Fermi energy) in the Coulomb potential case. At the Weyl point, the conductivity was calculated in the presence of short-range scatterers and it was found that the value of the minimum conductivity is $(e^2/h)\times(1/\pi)$ independently of disorder strength. The minimum conductivity is given by the product of e^2/h and a numerical factor ($=1/\pi$). It was thought that the minimum conductivity seems to be universal. However, in the Coulomb case it was found that the numerical factor multiplied by e^2/h is few times larger than the short-range case. Therefore, it was clarified that the minimum conductivity is not universal and depends on the impurity type. The minimum conductivity order of e^2/h was actually observed in the real transport measurement in graphene, and it was found that the value depends on the experimental condition. [31, 32, 33]

Then the natural question is: how the electronic transport looks like in 3D Weyl electron? In the 3D linear band, the density of states (DOS) near the Weyl point is proportional to $\varepsilon_{\rm F}^2$, and it is even more sparse than in $\varepsilon_{\rm F}$-linear DOS in the 2D Weyl case. The electronic transport in 3D Weyl electrons have been examined in several theoretical works. [1, 2, 22, 34, 35, 36, 37, 38, 39, 40, 41] There are theoretical calculations of the conductivity and the DOS at the Weyl point with the white-noise short-range scatters. The first work, Ref. [22], calculated the conductivity assuming the infinite degeneracy (i.e., infinite number of different Weyl points degenerate at a single energy), and it was found that there is a metal-insulator transition, where the system switches from insulating to metallic states when the disorder strength exceeds a certain critical value. The density of states in the Dirac semimetal was calculated in a recent work, [37] and the existence of the similar criti-

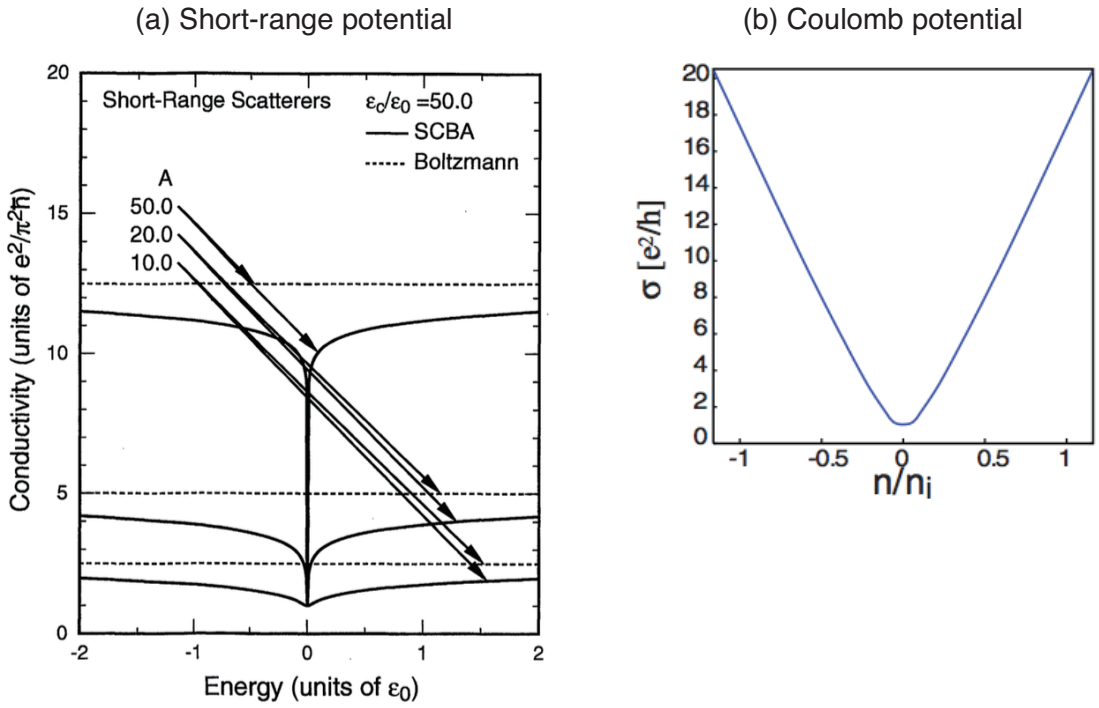

Figure 1.5: (a) The short-range potential case. [24] The panel shows the conductivity as a function of the Fermi energy. The conductivity is calculated within the SCBA and the Boltzmann theory for several scattering strength. (b) The Coulomb potential case. [29] The panel shows the conductivity as a function of the carrier density. The conductivity increases linearly with the increase of the carrier density. The carrier density is proportional to $\varepsilon_{\rm F}^2$, so that the conductivity is proportional to $\varepsilon_{\rm F}^2$. The conductivity is obtained by evaluating the finite-size Kubo formula.

cal behavior was obtained. Fig. 1.6 (a) and (b) show the conductivity and the DOS at the Weyl point as a function of the disorder strength and we see the metal-insulator transition. A related phase diagram was also presented in the context of the three-dimensional Z_2 quantum spin Hall system. [34] The electronic transport was also studied in recent works in terms of the frequency dependence of the dynamical conductivity. [36] The conductivity in the presence of the Coulomb scatterers was also argued within the Boltzmann transport theory in the energy region away from the Weyl point. [2, 36]

In the previous works, however, the transport property of the 3D Weyl electrons at the Weyl point was investigated by only using the short-range impurity potential, though the study on the transport of 2D Weyl electrons suggest that the transport property strongly depends on the type of impurity potential. The Coulomb potential case was investigated within the Boltzmann theory, but the Boltzmann fails at the Weyl point as we mention it in the previous paragraph. Therefore, it is not well known how the conductivity of 3D Weyl electrons behaves near the Weyl point in the presence of various kinds of impurity potentials.

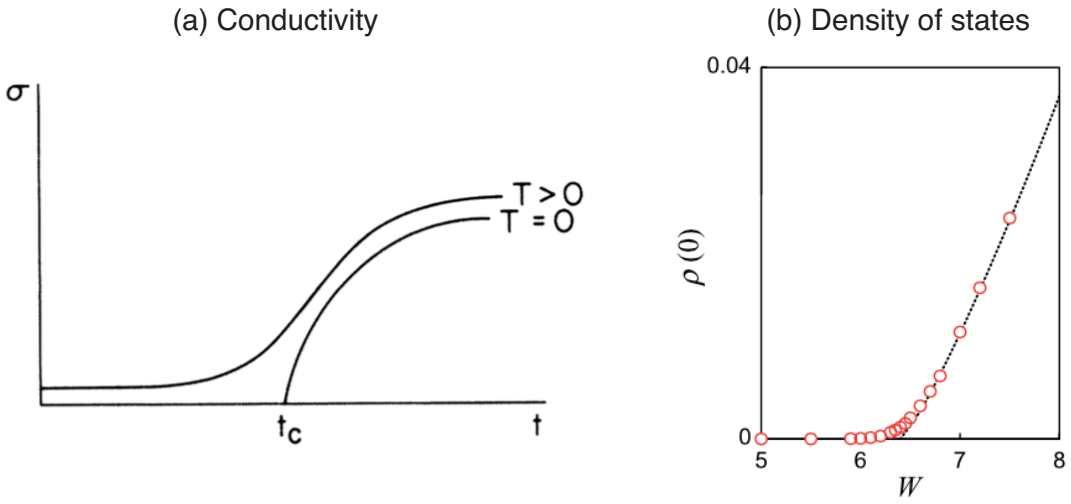

Figure 1.6: The conductivity and the DOS at the Weyl point as a function of the disorder strength. The conductivity in the degenerate point-nodes system at zero and finite temperature is shown in (a) [22], and the DOS in Dirac semimetal is in (b). [37] The conductivity and DOS vanish in the weak disorder, and once the disorder strength exceeds a certain critical value, they increase with the disorder strength. Around the critical value, we see the metal-insulator transition at a certain disorder strength.

1.2.2 Magnetotransport in Weyl semimetals

The transport of the Weyl semimetal in the magnetic field is also quite unusual, and this is closely related to the chiral anomaly in the quantum field theory. Fig. 1.7 shows the schematic energy spectrum of the Weyl semimetal under the magnetic field $\mathbf{B}$ parallel to z-axis, which is plotted against the momentum p_z. The left and right parts of the spectrum show the quantized Landau levels in the linear bands at $p_z = \pm p_0$, respectively. The 0th-Landau level is monotonically increasing in the left valley while decreasing in the right, i.e., the velocity in z-direction is positive in the left and negative in the right. The gradient (positive / negative) is determined by the helicity (right / left handed) of the corresponding point node, and it is shown that the numbers of left-handed and right-handed point nodes are always equal. Namely, we always have the same numbers of positive- and negative-velocity channels in total.

When ε_{F} is zero, the 0th Landau level is partially filled while other levels are fully occupied or empty. When a electric field $\mathbf{E}$ is applied to z-direction (parallel to the magnetic field), all the electrons shifts in p_z axis according to the semiclassical equation of motion $\dot{p_z} = -eE$, so that the Fermi energy goes down in the left valley while goes up in the right. This immediately leads to an imbalance of the electrons with positive velocity and with the nagetive velocity, causing the electric current in z-direction. The imbalance can be relaxed only by the inter-valley scattering. However, if the disorder potential is smooth enough that the matrix element connecting the two valleys are exponentially small, the conductivity in z-direction is expected to be exponentially large. This huge increase of the conductivity under $\mathbf{E} \parallel \mathbf{B}$ geometry was theoretically predicted by Nielsen and Ni-

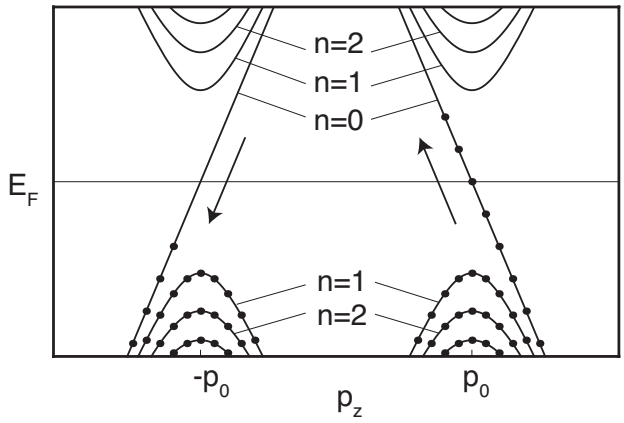

Figure 1.7: Schematic energy spectrum of Weyl semimetal in the presence of the magnetic field. Applying the electric field parallel to the z-axis ($\mathbf{E} \parallel \mathbf{B}$), we see the distribution imbalance between the two valleys, and the imbalance is relaxed by only the inter-valley scattering.

nomiya, in their early study on the Weyl fermion in crystals. [42, 43, 44] Motivated by the experimental discovery for Dirac and Weyl semimetals, the magnetotransport in these systems is investigated by several theoretical works. [45, 46, 47, 48, 49, 50, 51, 52] In particular, the semiclassical transport analysis for the Weyl semimetal showed the negative magnetoresistance (positive magnetoconductance) in proportion to B^2 in the weak field regime, i.e. the Landau level spacing is much smaller than the level broadening by the impurity potential and the temperature. [46, 47, 52] The magnetotransport in the strong field regime, i.e. only the 0th Landau level is relevant to the transport, is also investigated in recent works.[45, 48, 51] In the presence of the inter-valley scattering, it is obtained that the magnetoconductivity is independent of the magnetic field strength. An experimental signature of the B^2 dependence in the weak field was reported by several experimental groups. [53, 54, 55, 56, 57, 58, 59, 60] Fig. 1.8 shows the experimental data for the magnetoconductance.[60] We see the B^2 dependence of the conductance in $B \sim< 3$[T] under $\mathbf{E} \parallel \mathbf{B}$ geometry.

All the theoretical arguments above, however, assume bulk system and neglect the surface-boundary. What happens in realistic surface-boundary systems? In the presence of the surface-boundary, the topological surface states emerge as we mention it in the previous section. The topological surface states and the Fermi-arc are one of the most important properties of the Weyl semimetal and it must be appropriately incorporated also in arguing the transport phenomena.

1.3 Purpose and outline of this thesis

In this thesis, we study the quantum transport in the 3D Weyl electrons from the two viewpoints presented above.

In the first part (Chapter 2), we study the conductivity of 3D linear band under zero

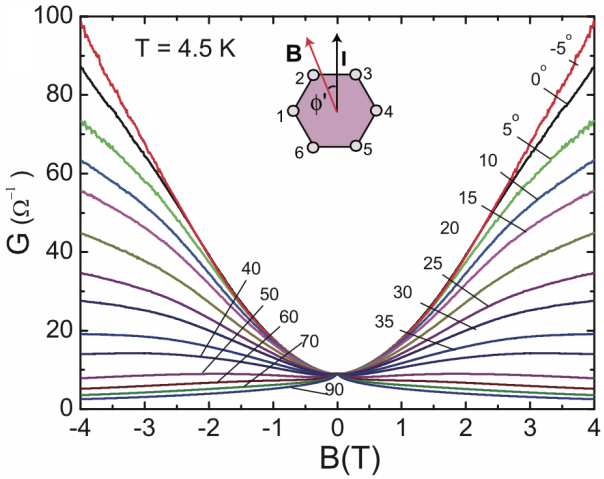

Figure 1.8: The experimental data for the conductance of Cd_3As_2 as a function of the magnetic field. The the conductance was measured in various angle between the electric field and the magnetic field. In $\mathbf{E} \parallel \mathbf{B}$ geometry, we see the B^2 dependence of the conductance in the weak magnetic field ($\sim< 3$[T]). [60]

magnetic field with various types of disorder potential. The previous works about the conductivity of 3D Weyl electrons at the Weyl point considered only the short-range scatterers, although the previous studies of 2D Weyl electrons strongly suggest that the transport property near the Weyl point is sensitive to the type of scattering potential. In addition to the works at the Weyl point, there are theoretical works considering another type of impurity potential, the Coulomb scatterers, but it consider the energy region away from the Weyl point. Therefore, the detailed behavior of the conductivity of 3D weyl electrons near the Weyl point in various types of scattering potential including long-range potential is not well known. The first purpose of this thesis is studying the electronic transport in 3D Weyl electrons with various types of disorder potential. The electronic state is described by the single-node Weyl Hamiltonian with the disorder potential. As the type of impurity potential affects the qualitative behavior of the conductivity, we consider two types of impurity potentials, a Gaussian potential and Coulomb potential. The Gaussian model mimics various disorder potential from the short-range scatters such as lattice defects to the long-range potential, by just changing the spacial range (smoothness) of the potential. The Coulomb potential serves as a realistic model for the charged impurities. Here we include the screening effect using the Thomas Fermi approximation. We clarify the detailed dependence of the conductivity on the scattering types and spatial range. We also clarify the dependence of the conductivity on the Fermi energy. We calculate the dc conductivity of 3D Weyl electrons using a self-consistent Born approximation (SCBA). The SCBA was used in the calculation of the conductivity of 2D Weyl [24, 30] and it is applicable to both zero and finite Fermi energy. Importantly, we show that the existence of the metal-insulator transition predicted in previous works depends on the types of the scatters: it occurs in Gaussian potential, while not in screened Coulomb case. We successfully described the mechanism of the transition using analytic approximation and specified

the criteria for the critical behavior in general impurity potential. We also closely study the Fermi energy dependence of the conductivity, and demonstrate that the conductivity gradually approaches the Boltzmann theory, when the Fermi energy becomes greater than the broadening energy.

In the second part (Chapter 3), we calculate the magneto-conductivity of the Weyl-semimetal with and without a surface-boundary. All previous works neglect the surface-boundary, so that the role of the topological surface states in the magnetotransport remains unknown. The second purpose of this thesis is to clarify how the surface states affect the magnetotransport. We consider the strong magnetic field regime where the 0th Landau level is relevant to the transport. We derive the band structure of the Weyl semimetal with the surface-boundary in the magnetic field and we clarify the role of the topological surface states in the giant magneto conductance in $\mathbf{E} \parallel \mathbf{B}$ geometry. We consider a simple lattice tight-binding model having a pair of point nodes at two isolated k-points, around which the electronic band structure is approximately described by the Weyl Hamiltonian. We assume a surface boundary and apply a magnetic field $\mathbf{B}$ in parallel to the surface, then we find that the surface band is seamlessly connected to the 0-th Landau level of the bulk spectrum, and form a closed single Fermi surface. For this situation, we calculate the conductivity under the electric field $\mathbf{E}$ parallel to $\mathbf{B}$, using the Boltzmann transport theory. Here the Fermi surface is not a point-like unlike the zero magnetic field and the Boltzmann transport theory is expected to be valid as long as the energy broadening is small. We show that the surface states play a crucial role in the magneto-conductance. Specifically, in the bulk system, the conductivity exponentially increases with the increase of the potential-range, reflecting the decrease of the inter-valley scattering probability. In the surface boundary system, on the other hand, such the exponential increase of the conductivity is completely suppressed due to the relaxation process mediated by the surface states. The magnetic-field dependence becomes also quite different between the periodic-boundary (bulk) and the surface boundary cases, where the bulk conductivity is independent of B while the surface-boundary conductivity linearly increases in B.

Finally, we present summary and conclusion in Chapter 4. We discuss the transport properties from the two viewpoints, the dc transport near the Weyl point and the magneto-transport in $\mathbf{E} \parallel \mathbf{B}$ geometry. We summarize our results in this thesis and give conclusions for the above problems.

Chapter 2

Quantum transport in single-node Weyl electrons

In this chapter, we calculate the bulk conductivity of 3D linear band. We consider a three-dimensional, single-node Weyl electron system described by a Hamiltonian,

$$\mathcal{H} = \hbar v \boldsymbol{\sigma} \cdot \boldsymbol{k} + \sum_j U(\boldsymbol{r} - \boldsymbol{r}_j), \tag{2.1}$$

where $\boldsymbol{\sigma} = (\sigma_x, \sigma_y, \sigma_z)$ is the Pauli matrices, $\boldsymbol{k}$ is a wave vector, v is a constant velocity. The second term is the long-range disorder potential, where $\boldsymbol{r}_j$ is the positions of randomly distributed scatterers. For the type of the disorder potential, we consider the Gaussian and the Coulomb type scatterer, and we separately argue them in Sec. 2.1 and 2.2 in nearly parallel manner.

2.1 Gaussian scatters

We introduce two types of long-ranged impurity potential. At first, we assume a long-ranged Gaussian potential for each single scatterers,

$$U(\boldsymbol{r}) = \frac{\pm u_0}{(\sqrt{\pi} d_0)^3} \exp\left(-\frac{r^2}{d_0^2}\right), \tag{2.2}$$

where d_0 is the characteristic length scale, and scatterers of $\pm u_0$ are randomly distributed with equal probability. This is Fourier transformed as $U(\boldsymbol{r}) = \int \mathrm{d}\boldsymbol{q} u(\boldsymbol{q}) e^{i\boldsymbol{q}\cdot\boldsymbol{r}}/(2\pi)^3$ where

$$u(\boldsymbol{q}) = \pm u_0 \exp\left(-\frac{q^2}{q_0^2}\right), \tag{2.3}$$

and $q_0 = 2/d_0$. We introduce an energy scale associated with the potential length scale,

$$\varepsilon_0 = \hbar v q_0. \tag{2.4}$$

and define a dimensionless parameter characterizing the scattering strength,

$$W = \frac{1}{4\pi} \frac{n_\mathrm{i} u_0^2 q_0}{\hbar^2 v^2}, \tag{2.5}$$

where n_i is the number of scatterers per unit volume.

2.1.1 Boltzmann transport theory

The Boltzmann transport equation for the distribution function $f_{s\boldsymbol{k}}$ is given by

$$-e\boldsymbol{E}\cdot\boldsymbol{v}_{s\boldsymbol{k}}\frac{\partial f_{s\boldsymbol{k}}}{\partial\varepsilon_{s\boldsymbol{k}}}=\sum_{s'}\int\frac{\mathrm{d}\boldsymbol{k}'}{(2\pi)^3}(f_{s'\boldsymbol{k}'}-f_{s\boldsymbol{k}})W_{s'\boldsymbol{k}',s\boldsymbol{k}}, \tag{2.6}$$

where $s=\pm1$ is a label for conduction and valence bands, and $W_{s'\boldsymbol{k}',s\boldsymbol{k}}$ is the scattering probability,

$$W_{s'\boldsymbol{k}',s\boldsymbol{k}}=\frac{2\pi}{\hbar}n_{\mathrm{i}}|\langle s'\boldsymbol{k}'|U|s\boldsymbol{k}\rangle|^2\delta(\varepsilon_{s'\boldsymbol{k}'}-\varepsilon_{s\boldsymbol{k}}). \tag{2.7}$$

The conductivity is obtained by solving Eq. (2.6). As usual manner, the transport relaxation time τ_{tr} is defined by

$$\frac{1}{\tau_{\mathrm{tr}}(\varepsilon_{s\boldsymbol{k}})}=\int\frac{\mathrm{d}\boldsymbol{k}'}{(2\pi)^3}(1-\cos\theta_{\boldsymbol{k}\boldsymbol{k}'})W_{s\boldsymbol{k}',s\boldsymbol{k}}, \tag{2.8}$$

where $\theta_{\boldsymbol{k}\boldsymbol{k}'}$ is the angle between $\boldsymbol{k}$ and $\boldsymbol{k}'$. For the isotropic scatterers, i.e., $u(\boldsymbol{q})$ depending only on $q=|\boldsymbol{q}|$, it is straightforward to show that $\tau_{\mathrm{tr}}(\varepsilon_{s\boldsymbol{k}})$ solely depends on the energy ε and written as [2]

$$\begin{aligned}\frac{1}{\tau_{\mathrm{tr}}(\varepsilon)}=&\frac{\pi}{\hbar}n_{\mathrm{i}}D_0(\varepsilon)\int_{-1}^{1}d(\cos\theta)\,u^2[2k\sin(\theta/2)]\\&\times(1-\cos\theta)\frac{1+\cos\theta}{2},\end{aligned} \tag{2.9}$$

where $k=\varepsilon/(\hbar v)$ and $D_0(\varepsilon)$ is the density of states in the ideal Weyl electrons,

$$D_0(\varepsilon)=\frac{\varepsilon^2}{2\pi^2(\hbar v)^3}. \tag{2.10}$$

The conductivity at $T=0$ is written as

$$\sigma_{\mathrm{B}}(\varepsilon)=e^2\frac{v^2}{3}D_0(\varepsilon)\tau_{\mathrm{tr}}(\varepsilon). \tag{2.11}$$

For the Gaussian scatter, Eq. (2.2), the relaxation time and conductivity are explicitly written as

$$\begin{aligned}\tau_{\mathrm{tr}}(\varepsilon)&=\frac{\hbar}{2\varepsilon_0 W}\,h\left(\frac{\varepsilon}{\varepsilon_0}\right),\\\sigma_{\mathrm{B}}(\varepsilon)&=\frac{1}{12\pi^2}\frac{e^2q_0}{\hbar}\frac{1}{W}\left(\frac{\varepsilon}{\varepsilon_0}\right)^2h\left(\frac{\varepsilon}{\varepsilon_0}\right),\end{aligned} \tag{2.12}$$

where

$$h(x)=\frac{64x^4}{4x^2-1+(4x^2+1)\exp(-8x^2)}. \tag{2.13}$$

In particular, the conductivity at the Weyl point is

$$\sigma_{\mathrm{B}}(0)=\frac{1}{8\pi^2}\frac{e^2q_0}{\hbar}\frac{1}{W}=\frac{1}{2\pi}\frac{e^2v^2\hbar}{n_{\mathrm{i}}u_0^2}, \tag{2.14}$$

which is independent of q_0. [2, 36] Fig. 2.1 shows the Boltzmann conductivity Eq. (2.12) as a function of the Fermi energy.

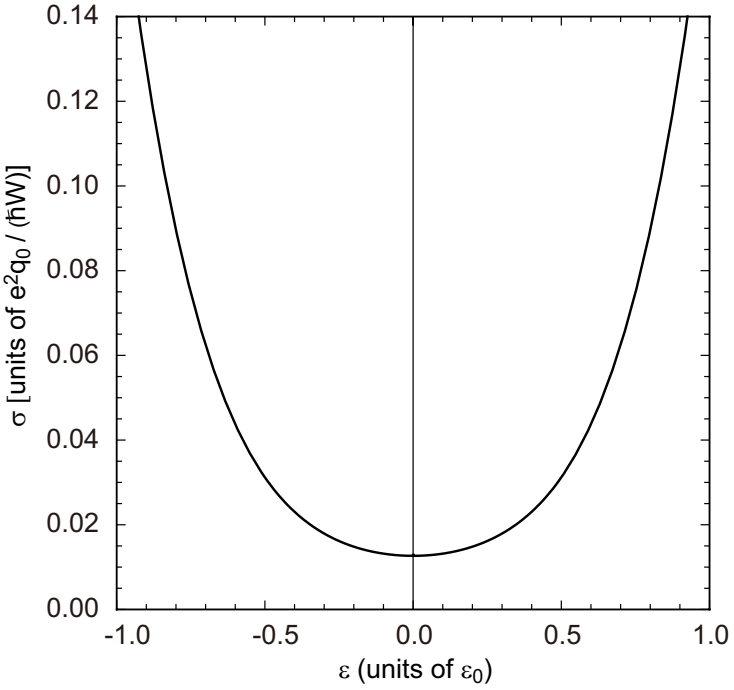

Figure 2.1: Boltzmann conductivity [Eq. (2.12)] plotted as a function of the Fermi energy.

2.1.2 Self-consistent Born approximation (SCBA)

We introduce the self-consistent Born approximation (SCBA) for 3D Weyl electron in a similar manner to the 2D version in Ref. [30]. The following formulation does not depend on the specific form of the single impurity potential $U(\boldsymbol{r})$, as long as it is isotropic. We define the averaged Green's function as

$$\hat{G}(\boldsymbol{k},\varepsilon) = \left\langle \frac{1}{\varepsilon - \mathcal{H}} \right\rangle = \frac{1}{\varepsilon - \hbar v \boldsymbol{\sigma}\cdot\boldsymbol{k} - \hat{\Sigma}(\boldsymbol{k},\varepsilon)}, \tag{2.15}$$

where $\langle \cdots \rangle$ represents the average over the configuration of the impurity position. $\hat{\Sigma}(\boldsymbol{k},\varepsilon)$ is the self-energy matrix, which is approximated in SCBA as

$$\hat{\Sigma}(\boldsymbol{k},\varepsilon) = \int \frac{\mathrm{d}\boldsymbol{k}'}{(2\pi)^3} n_{\mathrm{i}} |u(\boldsymbol{k}-\boldsymbol{k}')|^2 \hat{G}(\boldsymbol{k}',\varepsilon). \tag{2.16}$$

Eqs. (2.15) and (2.16) are a set of equations to be solved self-consistently. From the symmetry of the present system, the self-energy matrix can be expressed as

$$\hat{\Sigma}(\boldsymbol{k},\varepsilon) = \Sigma_1(k,\varepsilon) + \Sigma_2(k,\varepsilon)(\boldsymbol{\sigma}\cdot\boldsymbol{n}), \tag{2.17}$$

where $k = |\boldsymbol{k}|$ and $\boldsymbol{n} = \boldsymbol{k}/k$. By defining $X(k,\varepsilon)$ and $Y(k,\varepsilon)$ as

$$X(k,\varepsilon) = \varepsilon - \Sigma_1(k,\varepsilon), \tag{2.18}$$

$$Y(k,\varepsilon) = \hbar v k + \Sigma_2(k,\varepsilon), \tag{2.19}$$

Eqs. (2.15) and (2.16) are written as

$$\hat{G}(\boldsymbol{k},\varepsilon) = \frac{1}{X(k,\varepsilon) - Y(k,\varepsilon)(\boldsymbol{\sigma}\cdot\boldsymbol{n})}, \tag{2.20}$$

and

$$\hat{\Sigma}(\boldsymbol{k},\varepsilon) = \int \frac{\mathrm{d}\boldsymbol{k}'}{(2\pi)^3} n_{\mathrm{i}} |u(\boldsymbol{k}-\boldsymbol{k}')|^2 \frac{X' + Y'(\boldsymbol{\sigma}\cdot\boldsymbol{n}')}{X'^2 - Y'^2}, \tag{2.21}$$

where $X' = X(k',\varepsilon)$, $Y' = Y(k',\varepsilon)$, and $\boldsymbol{n}' = \boldsymbol{k}'/k'$.

Now, we divide $\boldsymbol{n}'$ as

$$\boldsymbol{n}' = \boldsymbol{n}'_{\parallel} + \boldsymbol{n}'_{\perp}, \tag{2.22}$$

where $\boldsymbol{n}'_{\parallel} = (\boldsymbol{n}\cdot\boldsymbol{n}')\boldsymbol{n}$ is the component of parallel to $\boldsymbol{n}$, and $\boldsymbol{n}'_{\perp}$ is the perpendicular part. Then Eq. (2.21) becomes

$$\begin{aligned}\hat{\Sigma}(\boldsymbol{k},\varepsilon) = &\int \frac{\mathrm{d}\boldsymbol{k}'}{(2\pi)^3} n_{\mathrm{i}} |u(\boldsymbol{k}-\boldsymbol{k}')|^2 \frac{X'}{X'^2 - Y'^2} \\ &+ \int \frac{\mathrm{d}\boldsymbol{k}'}{(2\pi)^3} n_{\mathrm{i}} |u(\boldsymbol{k}-\boldsymbol{k}')|^2 \frac{Y'}{X'^2 - Y'^2} (\boldsymbol{\sigma}\cdot\boldsymbol{n}'_{\parallel}) \\ &+ \int \frac{\mathrm{d}\boldsymbol{k}'}{(2\pi)^3} n_{\mathrm{i}} |u(\boldsymbol{k}-\boldsymbol{k}')|^2 \frac{Y'}{X'^2 - Y'^2} (\boldsymbol{\sigma}\cdot\boldsymbol{n}'_{\perp}).\end{aligned} \tag{2.23}$$

The third term vanishes after the integration over the $\boldsymbol{k}'$ direction, giving

$$\begin{aligned}\hat{\Sigma}(\boldsymbol{k},\varepsilon) = &\int_0^\infty \frac{k'^2 \mathrm{d}k'}{(2\pi)^3} n_{\mathrm{i}} V_0^2(k,k') \frac{X'}{X'^2 - Y'^2} \\ &+ (\boldsymbol{\sigma}\cdot\boldsymbol{n}) \int_0^\infty \frac{k'^2 \mathrm{d}k'}{(2\pi)^3} n_{\mathrm{i}} V_1^2(k,k') \frac{Y'}{X'^2 - Y'^2},\end{aligned} \tag{2.24}$$

where

$$V_n^2(k,k') = 2\pi \int_{-1}^{1} \mathrm{d}(\cos\theta_{\boldsymbol{k}\boldsymbol{k}'}) |u(\boldsymbol{k}-\boldsymbol{k}')|^2 \cos^n\theta_{\boldsymbol{k}\boldsymbol{k}'}. \tag{2.25}$$

Eq. (2.24) immediately leads to the self-consistent equation,

$$X(k,\varepsilon) = \varepsilon - \int_0^\infty \frac{k'^2 \mathrm{d}k'}{(2\pi)^3} n_{\mathrm{i}} V_0^2(k,k') \frac{X'}{X'^2 - Y'^2}, \tag{2.26}$$

$$Y(k,\varepsilon) = \hbar v k + \int_0^\infty \frac{k'^2 \mathrm{d}k'}{(2\pi)^3} n_{\mathrm{i}} V_1^2(k,k') \frac{Y'}{X'^2 - Y'^2}, \tag{2.27}$$

which are to be solved numerically. From the obtained Green's function, the density of states per unit area is calculated as

$$D(\varepsilon) = -\frac{1}{\pi} \mathrm{Im} \int \frac{\mathrm{d}\boldsymbol{k}}{(2\pi)^3} \mathrm{Tr}[\hat{G}(\boldsymbol{k},\varepsilon + i0)]. \tag{2.28}$$

The Kubo formula for the conductivity is given by

$$\sigma(\varepsilon) = -\frac{\hbar e^2 v^2}{4\pi} \sum_{s,s'=\pm 1} ss' \int \frac{\mathrm{d}\boldsymbol{k}'}{(2\pi)^3} \mathrm{Tr}\Big[\sigma_x \hat{G}(\boldsymbol{k}', \varepsilon + is0) \times \hat{J}_x(\boldsymbol{k}', \varepsilon + is0, \varepsilon + is'0)\hat{G}(\boldsymbol{k}', \varepsilon + is'0)\Big], \tag{2.29}$$

where $\hat{J}_x$ is current vertex-part satisfying the Bethe-Salpeter equation

$$\hat{J}_x(\boldsymbol{k}, \varepsilon, \varepsilon') = \sigma_x + \int \frac{\mathrm{d}\boldsymbol{k}'}{(2\pi)^3} n_\mathrm{i} |u(\boldsymbol{k} - \boldsymbol{k}')|^2 \hat{G}(\boldsymbol{k}', \varepsilon) \times \hat{J}_x(\boldsymbol{k}', \varepsilon, \varepsilon')\hat{G}(\boldsymbol{k}', \varepsilon'). \tag{2.30}$$

To calculate this, we consider an integral

$$I(\boldsymbol{k}) = \int \frac{\mathrm{d}\boldsymbol{k}'}{(2\pi)^3} |u(\boldsymbol{k} - \boldsymbol{k}')|^2 F(k')(\boldsymbol{\sigma} \cdot \boldsymbol{n}')\sigma_x(\boldsymbol{\sigma} \cdot \boldsymbol{n}'), \tag{2.31}$$

where $F(k)$ is an arbitrary function. After some algebra, we have

$$\begin{aligned} I(\boldsymbol{k}) =& \sigma_x \int \frac{k'^2 \mathrm{d}k'}{(2\pi)^3} F(k') \left(-\frac{1}{2} V_0^2(k, k') + \frac{1}{2} V_2^2(k, k') \right) \\ &+ (\boldsymbol{\sigma} \cdot \boldsymbol{n})\sigma_x(\boldsymbol{\sigma} \cdot \boldsymbol{n}) \int \frac{k'^2 \mathrm{d}k'}{(2\pi)^3} F(k') \\ &\times \left(-\frac{1}{2} V_0^2(k, k') + \frac{3}{2} V_2^2(k, k') \right). \end{aligned} \tag{2.32}$$

In a similar way as for the self-energy, we obtain

$$\begin{aligned} &\int \frac{\mathrm{d}\boldsymbol{k}'}{(2\pi)^3} |u(\boldsymbol{k} - \boldsymbol{k}')|^2 F(k')(\boldsymbol{\sigma} \cdot \boldsymbol{n}')\sigma_x \\ &\quad = (\boldsymbol{\sigma} \cdot \boldsymbol{n})\sigma_x \int \frac{k'^2 \mathrm{d}k'}{(2\pi)^3} F(k') V_1^2(k, k'), \\ &\int \frac{\mathrm{d}\boldsymbol{k}'}{(2\pi)^3} |u(\boldsymbol{k} - \boldsymbol{k}')|^2 F(k')\sigma_x(\boldsymbol{\sigma} \cdot \boldsymbol{n}') \\ &\quad = \sigma_x(\boldsymbol{\sigma} \cdot \boldsymbol{n}) \int \frac{k'^2 \mathrm{d}k'}{(2\pi)^3} F(k') V_1^2(k, k'). \end{aligned} \tag{2.33}$$

Using these, the vertex part $\hat{J}$ is written as

$$\begin{aligned} \hat{J}_x(\boldsymbol{k}, \varepsilon, \varepsilon') =& \sigma_x J_0(k, \varepsilon, \varepsilon') + (\boldsymbol{\sigma} \cdot \boldsymbol{n})\sigma_x(\boldsymbol{\sigma} \cdot \boldsymbol{n}) J_1(k, \varepsilon, \varepsilon') \\ &+ (\boldsymbol{\sigma} \cdot \boldsymbol{n})\sigma_x J_2(k, \varepsilon, \varepsilon') + \sigma_x(\boldsymbol{\sigma} \cdot \boldsymbol{n}) J_3(k, \varepsilon, \varepsilon'), \end{aligned} \tag{2.34}$$

and the Bethe-Salpeter equation becomes

$$\begin{aligned}\begin{pmatrix} J_0 \\ J_1 \\ J_2 \\ J_3 \end{pmatrix} = \begin{pmatrix} 1 \\ 0 \\ 0 \\ 0 \end{pmatrix} + \int_0^\infty \frac{k'^2 \mathrm{d}k'}{(2\pi)^3} \frac{n_\mathrm{i}}{(X^2 - Y^2)(X'^2 - Y'^2)} \\ \times \begin{pmatrix} V_0^2 & -(V_0^2 - V_2^2)/2 & 0 & 0 \\ 0 & -(V_0^2 - 3V_2^2)/2 & 0 & 0 \\ 0 & 0 & V_1^2 & 0 \\ 0 & 0 & 0 & V_1^2 \end{pmatrix} \\ \times \begin{pmatrix} XX' & YY' & YX' & XY' \\ YY' & XX' & XY' & YX' \\ YX' & XY' & XX' & YY' \\ XY' & YX' & YY' & XX' \end{pmatrix} \begin{pmatrix} J_0' \\ J_1' \\ J_2' \\ J_3' \end{pmatrix}, \end{aligned} \tag{2.35}$$

where $X = X(k', \varepsilon)$, $X' = X(k', \varepsilon')$, $J_0 = J_0(k, \varepsilon, \varepsilon')$, $J_0' = J_0(k', \varepsilon, \varepsilon')$, etc. Finally, the conductivity is written as

$$\begin{aligned}\sigma(\varepsilon) =& \frac{4\hbar e^2 v^2}{3} \int_0^\infty \frac{k^2 \mathrm{d}k}{(2\pi)^3} \\ & \times \mathrm{Re}\Bigg[\frac{1}{|X^2 - Y^2|^2} \\ & \quad \times \Big\{ (3|X|^2 - |Y|^2) J_0^{+-} + (3|Y|^2 - |X|^2) J_1^{+-} \\ & \qquad + (3YX^* - XY^*) J_2^{+-} + (3XY^* - YX^*) J_3^{+-} \Big\} \\ & \quad - \frac{1}{(X^2 - Y^2)^2} \\ & \quad \times \Big\{ (3X^2 - Y^2) J_0^{++} + (3Y^2 - X^2) J_1^{++} \\ & \qquad + 2XY J_2^{++} + 2XY J_3^{++} \Big\} \Bigg], \end{aligned} \tag{2.36}$$

where $X = X(k, \varepsilon + i0)$, $J_0^{ss'} = J_0(k, \varepsilon + is0, \varepsilon + is'0)$, etc.

2.1.3 Approximate analytical solution of SCBA

In this section, we derive an approximate analytical solution of the SCBA equation in the previous section. Near $\varepsilon = 0$, we can derive an approximate analytical solution of the SCBA equation in the previous section, as long as the level broadening $\Gamma(\varepsilon)$ is much smaller than ε_0. There we replace $u(q)$ with the constant u_0 (i.e., short-ranged impurity), but, instead, introduce a cutoff $k_\mathrm{c} \sim q_0$ in the k-space integral to simulate the exponential decay of $u(q)$ in a large q. The approximation is rather crude, while it effectively explains the qualitative behavior peculiar to the 3D Weyl electron as shown in the following section.

In this simplified system (short-range impurities with cutoff), the self-energy equation Eq. (2.16) is approximately solved in $\varepsilon \ll \varepsilon_{\rm c}$ and $\Gamma \ll \varepsilon_{\rm c}$ as

$$\hat{\Sigma}(\boldsymbol{k}, \varepsilon) \approx (1-\alpha)\varepsilon - i\Gamma(\varepsilon), \tag{2.37}$$

where

$$\begin{aligned} \Gamma(\varepsilon) &= \frac{\Gamma_W}{2} + \sqrt{\left(\frac{\Gamma_W}{2}\right)^2 + \alpha^2\varepsilon^2}, \\ \alpha &= \left(1 - \frac{W}{W_{\rm c}}\right)^{-1}, \\ \Gamma_W &= \varepsilon_0 \left(\frac{1}{W_{\rm c}} - \frac{1}{W}\right), \end{aligned} \tag{2.38}$$

and

$$W_{\rm c} = \frac{\pi}{2}\frac{\varepsilon_0}{\varepsilon_{\rm c}}, \tag{2.39}$$

where $\varepsilon_{\rm c} = \hbar v k_{\rm c}$ is the cut-off energy. The density of states is then written in terms of $\Gamma(\varepsilon)$ as

$$D(\varepsilon) = \frac{\varepsilon_0}{2\pi^2(\hbar v)^3}\frac{\Gamma(\varepsilon)}{W}. \tag{2.40}$$

At $\varepsilon = 0$, in particular, $\Gamma(\varepsilon)$ becomes

$$\Gamma(0) = \begin{cases} 0 & (W < W_{\rm c}) \\ \Gamma_W & (W > W_{\rm c}) \end{cases}, \tag{2.41}$$

i.e., the self-energy, and thus the density of states, become zero in the weak disorder regime $W < W_{\rm c}$, and abruptly rise in the strong disorder regime $W > W_{\rm c}$. The vanishing $\Gamma(0)$ at a finite W is peculiar to three dimensions, and it is intuitively understood as follows. By assuming a solution of the form Eq. (2.37), the Eq. (2.26) can be written at $\varepsilon = 0$ as

$$\Gamma = \frac{n_{\rm i}u_0^2}{2\pi^2}\int_0^{k_{\rm c}} k^2 {\rm d}k \frac{\Gamma}{(\hbar v k)^2 + \Gamma^2}, \tag{2.42}$$

which is to be solved for Γ. For a non-zero Γ, it becomes

$$1 = \frac{n_{\rm i}u_0^2}{2\pi^2}\int_0^{k_{\rm c}} k^2 {\rm d}k \frac{1}{(\hbar v k)^2 + \Gamma^2}. \tag{2.43}$$

When the right-hand side of Eq. (2.43) is viewed as a function of Γ, it has an upper bound $n_{\rm i}u_0^2 k_{\rm c}/(2\pi^2\hbar^2 v^2)$, which is achieved at $\Gamma = 0$. When the scattering strength is so small that $n_{\rm i}u_0^2 k_{\rm c}/(2\pi^2\hbar^2 v^2)$ is smaller than 1, Eq. (2.43) has no solution, and we are left only with a trivial solution $\Gamma = 0$ in Eq. (2.42). This critical condition exactly corresponds to $W < W_{\rm c}$. In contrast, the self-consistent equation in 2D always has a non-zero solution

for any scattering strength, [24] because in Eq. (2.43), $k^2\mathrm{d}k$ is replaced with $k\mathrm{d}k$, and then the right-hand side logarithmically diverges in $\Gamma \to 0$, giving no upper bound.

In a similar manner, the Bethe-Salpeter equation Eq. (2.35) is approximately solved as

$$\begin{pmatrix} J_0 \\ J_1 \\ J_2 \\ J_3 \end{pmatrix} \approx \begin{pmatrix} J \\ 0 \\ 0 \\ 0 \end{pmatrix}, \tag{2.44}$$

where

$$J = \left[1 + \frac{1}{3}\frac{W}{W_\mathrm{c}}\right]^{-1}. \tag{2.45}$$

The conductivity is obtained as

$$\sigma(\varepsilon) = \frac{J}{12\pi^2}\frac{e^2}{\hbar}\frac{1}{\hbar v}\frac{3\Gamma(\varepsilon)^2 + \alpha^2\varepsilon^2}{\Gamma(\varepsilon)}. \tag{2.46}$$

When $\Gamma(0)$ is non-zero, the conductivity at $\varepsilon = 0$ can be simply obtained by replacing $\Gamma(\varepsilon)$ with $\Gamma(0)$ as

$$\sigma(0) = \frac{J}{4\pi^2}\frac{e^2}{\hbar}\frac{\Gamma(0)}{\hbar v}. \tag{2.47}$$

In the strong disorder regime $W > W_\mathrm{c}$, this gives

$$\sigma(0) = \frac{J}{12\pi^2}\frac{e^2 q_0}{\hbar} \times 3\left(\frac{1}{W_\mathrm{c}} - \frac{1}{W}\right) \quad (W > W_\mathrm{c}). \tag{2.48}$$

In the weak disorder regime $W < W_\mathrm{c}$, Eq. (2.47) is no longer valid since $\Gamma(0) = 0$, and then we need to take a limit $\varepsilon \to 0$ to consider $\sigma(0)$. We expand $\Gamma(\varepsilon)$ in Eq. (2.38) as

$$\Gamma(\varepsilon) \approx \frac{\alpha^2\varepsilon^2}{|\Gamma_W|} \quad (W < W_\mathrm{c}), \tag{2.49}$$

and obtain

$$\lim_{\varepsilon\to 0}\sigma(\varepsilon) = \frac{J}{12\pi^2}\frac{e^2 q_0}{\hbar} \times \left(\frac{1}{W} - \frac{1}{W_\mathrm{c}}\right) \quad (W < W_\mathrm{c}). \tag{2.50}$$

From Eqs. (2.48) and (2.50), we see that the Weyl-point conductivity $\sigma(0)$ vanishes at $W = W_\mathrm{c}$, and it increases as W goes away from W_c in either direction.

In the vicinity of the critical point $W = W_\mathrm{c}$, α becomes large and $\Gamma(\varepsilon)$ and $\sigma(\varepsilon)$ approximate linear functions,

$$\begin{aligned} \Gamma(\varepsilon) &\approx |\alpha\varepsilon| \\ \sigma(\varepsilon) &\approx \frac{1}{4\pi^2}\frac{e^2}{\hbar}\frac{|\alpha\varepsilon|}{\hbar v} \end{aligned} \quad (W \approx W_\mathrm{c}), \tag{2.51}$$

of which gradient diverges at $W = W_\mathrm{c}$.

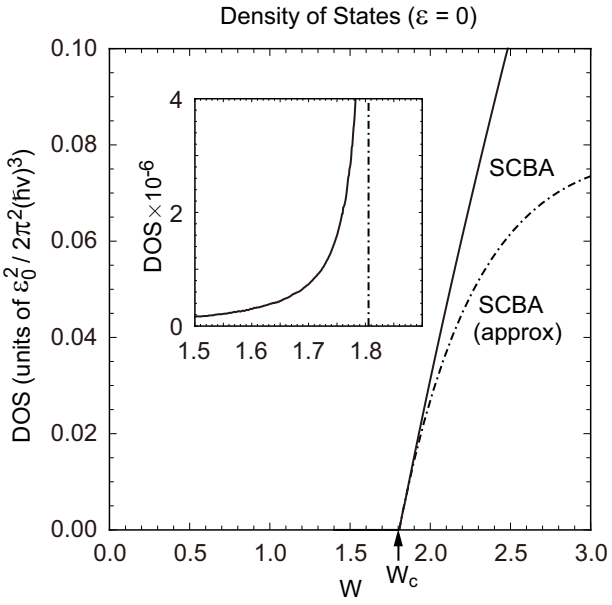

Figure 2.2: (Solid) Density of states at zero energy calculated by the SCBA. (Dotted-dashed) Approximate expression Eq. (2.40) with Eq. (2.38), where $\varepsilon_c/\varepsilon_0$ is taken as 0.87. Inset shows the density of states near $W_c \approx 1.806$ in a smaller scale.

2.1.4 Numerical solution of SCBA

We solve the SCBA equations Eq. (2.26), (2.27),and (2.35) by numerical iteration and calculate the density of states and the conductivity. Fig. 2.2 shows the density of states at $\varepsilon = 0$ as a function of W. The behavior is qualitatively similar to the approximate analysis in the previous section. There is a critical disorder strength $W_c \approx 1.806$, and the density of states rapidly increases once W enters the strong disorder regime $W > W_c$. The dotted-dashed line in Fig. 2.2 shows the approximate SCBA solution of Eq. (2.40) at $\varepsilon = 0$, where $\varepsilon_c/\varepsilon_0$ is taken as ≈ 0.87 to fit W_c to the numerically obtained value. It nicely reproduces the increase in $W > W_c$, though the approximation fails in larger W because the assumption $\Gamma \ll \varepsilon_c$ in deriving Eq. (2.38) becomes no longer valid as Γ increases. Actually, the density of states in the weak disorder regime $W < W_c$ does not completely vanish in the numerics unlike the analytic approximation, but an exponentially small value remains as shown in the inset in Fig. 2.2. The rapid increase in $W < W_c$ is roughly expressed by $\propto 1/(W_c - W)$. As we will argue later, this small residue leads to a significant difference in the zero-energy conductivity between the numerical calculation and the analytic approximation.

Figs. 2.3 (a) and (b) show the density of states and the conductivity as a function of the Fermi energy, respectively, which are numerically calculated by the SCBA. Figs. 2.3 (c) and (d) are the detailed plots around zero energy for Figs. 2.3 (a) and (b), respectively. We see that the density of states is enhanced in all the energy region with the increase of the scattering strength W. In the weak disorder regime $W < W_c$, it approximates a quadratic curve in the vicinity of $\varepsilon = 0$, and it nearly sticks to zero at the origin. At the critical point W_c, the curve exhibits a wedge-like shape, and in the strong disorder regime

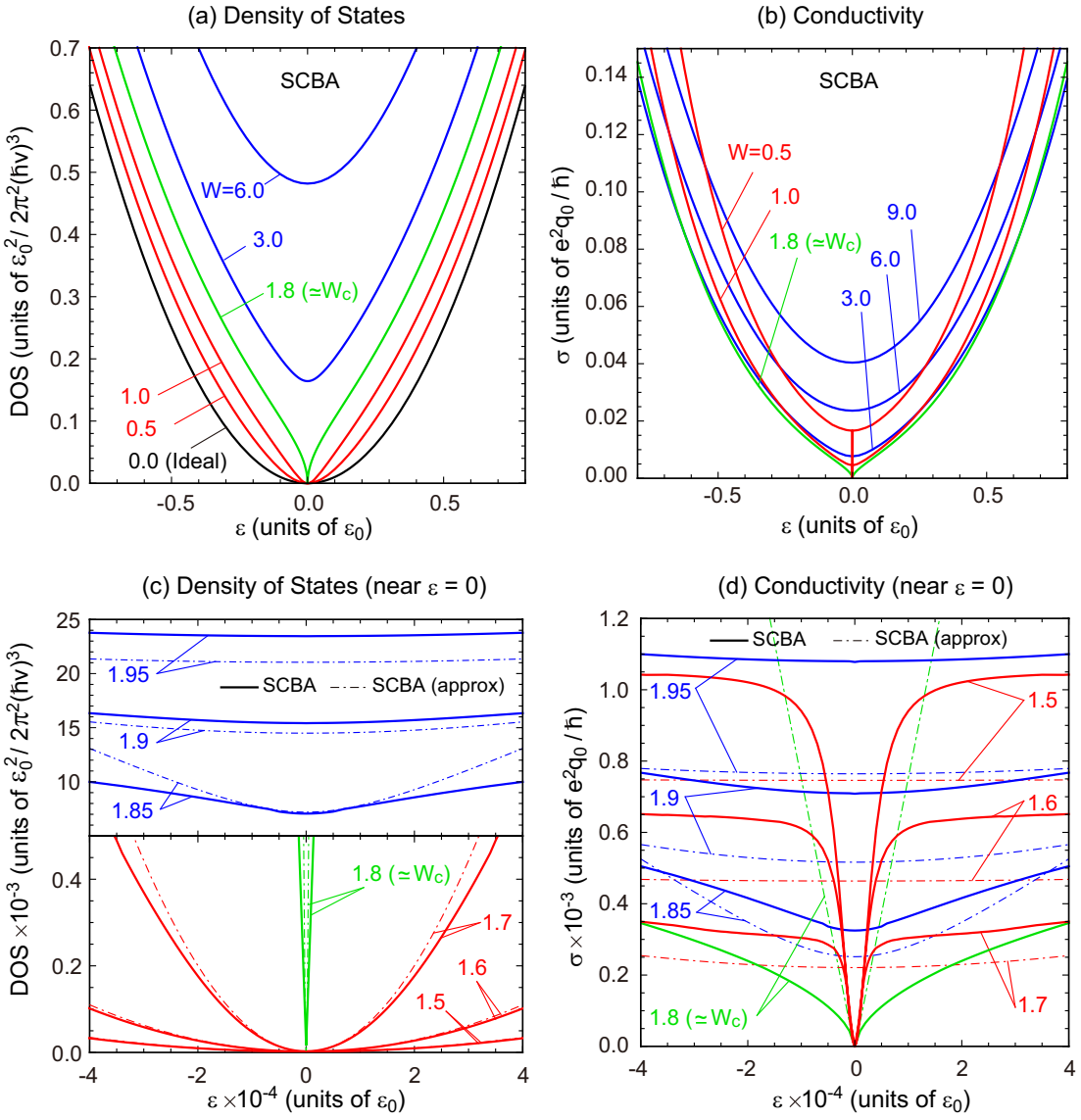

Figure 2.3: Density of states (a,c) and the conductivity (b,d) calculated by the SCBA, as a function of the Fermi energy. The panels (c) and (d) show the detailed plots near $\varepsilon = 0$ of (a) and (b), respectively. The dotted-dashed line in Fig. 2.3(c) and (d) represent the approximate SCBA solution, Eq. (2.40) and Eq. (2.46), respectively.

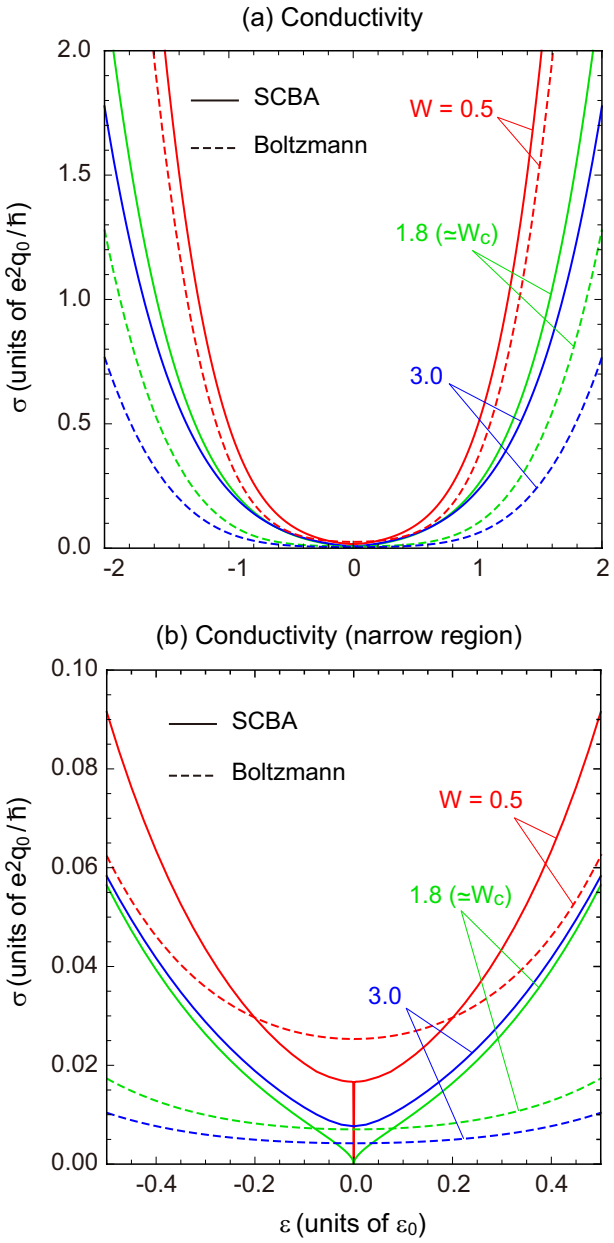

Figure 2.4: SCBA conductivity and the Boltzmann conductivity [Eq. (2.12)] at several W's plotted for (a) wide and (b) narrow energy regions.

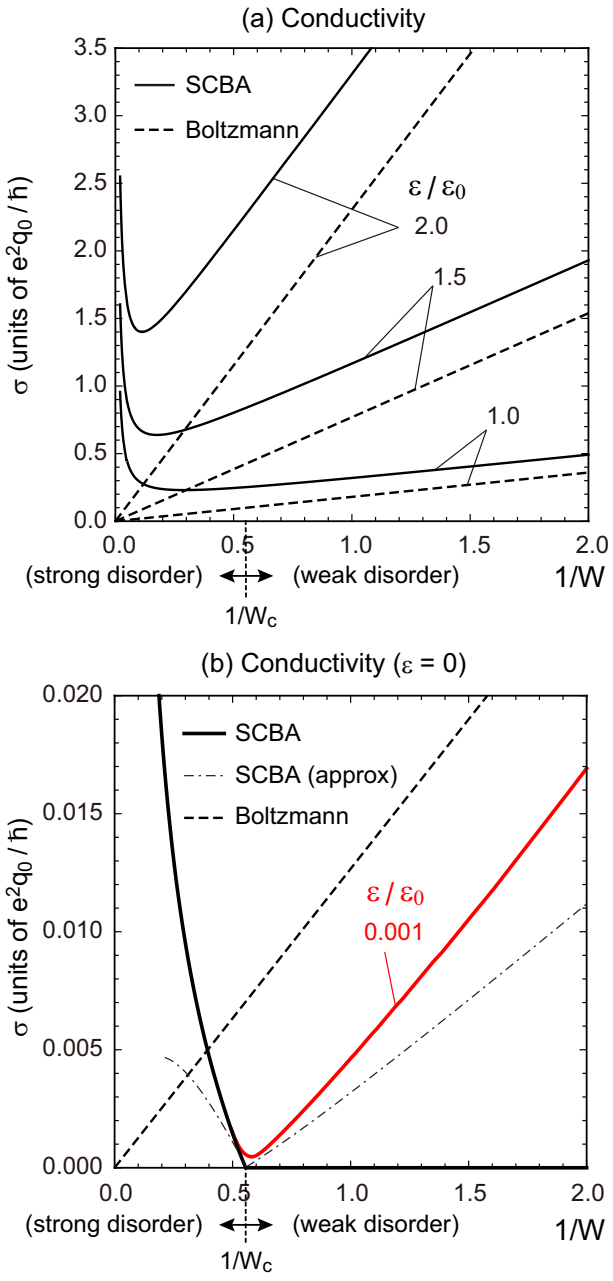

Figure 2.5: (a) SCBA conductivity (solid) and the Boltzmann conductivity (dashed) as a function of $1/W$, for some fixed Fermi energies. (b) A similar plot for small Fermi energies, $\varepsilon = 0$ and $0.001\varepsilon_0$. Dotted-dashed line represents the approximate SCBA solution, Eqs. (2.48) and (2.50) at $\varepsilon = 0$.

$W > W_c$, the bottom of the curve departs from zero as already argued. The dotted-dashed line in Fig. 2.3(c) represents the approximate SCBA solution near zero energy, Eq. (2.40). It reproduces the qualitative behavior of the numerical curve. At $W = 1.8$, slightly away from the critical point $W_c \approx 1.806$, the density of states is approximated by a linear function in accordance with Eq. (2.51).

The conductivity exhibits significantly different behaviors between the weak and strong disorder regimes. In Fig. 2.4, we compare the SCBA conductivity and the Boltzmann conductivity Eq. (2.12) at several W's in (a) wide and (b) narrow energy regions. We see that the SCBA agrees well with the Boltzmann conductivity in small W, while the discrepancy becomes significant as W increases. The Boltzmann theory works well when the condition that the self-energy is much smaller than the Fermi energy, so that the theory naturally stands in the weak disorder regime. In the strong disorder regime $W > W_c$, the Boltzmann approximation fails and the SCBA conductivity is *enhanced* in increasing W as observed in Figs. 2.3 (b) and (d), contrary to the usual metallic behavior. When W is too strong the SCBA is no longer valid and the correction from the quantum interference effect would be important.

In the weak disorder regime $W < W_c$, we notice that the conductivity $\sigma(\varepsilon)$ exhibits a sharp dip at the zero energy, as shown in Fig. 2.3(d) in a greater scale. The dotted-dashed line in Fig. 2.3(d) indicates the approximate SCBA solution near zero energy, Eq. (2.46), with $\varepsilon_c/\varepsilon_0 = 0.87$ (the same value used in the DOS plot). We see that the analytic approximation fails to describe the zero-energy dip observed in the numerics, while, in the flat region outside the dip, the approximation qualitatively reproduces the W-dependence of the numerical conductivity.

The conductivity dip actually originates from an exponentially small self-energy remaining at $\varepsilon = 0$, which is missing in the analytic approximation. Indeed, the entire curve including the dip is qualitatively reproduced by Eq. (2.46), when $\Gamma(\varepsilon)$ of Eq. (2.49) is modified by

$$\Gamma(\varepsilon) \approx \Gamma_{\rm num} + \frac{\alpha^2\varepsilon^2}{|\Gamma_W|} \quad (W < W_c), \tag{2.52}$$

where $\Gamma_{\rm num}$ is the small residue of the selfenergy at $\varepsilon = 0$ in the numerical calculation. The conductivity $\sigma(0)$ is then given by Eq. (2.47), and thus is exponentially small. In increasing the Fermi energy ε, $\Gamma_{\rm num}$ becomes less important in Eq. (2.52), and the conductivity gradually approaches the original analytic expression Eq. (2.50). The energy width of the dip is roughly estimated by the condition $\alpha^2\varepsilon^2/|\Gamma_W| \sim \Gamma_{\rm num}$.

In Fig. 2.5(a), the SCBA conductivity (solid) and the Boltzmann conductivity (dashed) at fixed Fermi energies are plotted as a function of $1/W$ (not W). In the weak disorder regime ($W < W_c$), the SCBA conductivity is proportional to $1/W$, and it coincides nicely with the Boltzmann conductivity Eq. (2.62) except for a constant shift. In increasing the disorder (i.e., decreasing $1/W$), on the other hand, the SCBA conductivity reaches a minimum at a certain point, and it turns to increase nearly in proportional to W. The scattering strength for the turning point is of the order of W_c, and moves toward larger W (i.e., smaller $1/W$) for larger Fermi energy.

Fig. 2.5(b) presents a similar plot at zero energy, where the approximate SCBA solution, Eqs. (2.48) and (2.50), is plotted as a dotted-dashed line. We also show the numerical SCBA

conductivity at $\varepsilon = 0.001\varepsilon_0$, slightly away from the Weyl point. In the weak disorder regime ($W < W_c$), the SCBA conductivity is very sensitive to ε as expected from the sharp dip structure in Fig. 2.3(d). The energies $\varepsilon = 0$ and $\varepsilon = 0.001\varepsilon_0$ correspond to the bottom of the dip and the flat region outside the dip, respectively. The conductivity in $W < W_c$ is exponentially small at $\varepsilon = 0$ as already argued, while at $\varepsilon = 0.001\varepsilon_0$ it linearly rises approximately in accordance with the analytical expression Eq. (2.50). In the strong disorder regime ($W > W_c$), the SCBA conductivity is almost identical between the two different energies, and goes up nearly in accordance with Eq. (2.48).

In 3D Weyl electron, the Weyl-point conductivity is highly W-dependent since Eq. (2.47) is proportional to $\Gamma(0)$, and it abruptly rises when W exceeds W_c just in the same way as the density of states. This is in a sharp contrast to the 2D case, where the Weyl-point conductivity becomes nearly universal value of the order of e^2/h. [23, 24, 25, 27, 26, 30, 22] The 3D Weyl system does not have such a universal conductivity, because the conductivity in 3D has a dimension of e^2/h times the inverse of the length scale, and this is given by $\Gamma(0)/(\hbar v)$ in the present system.

2.2 Coulomb potential

Next, we assume a long-ranged screened Coulomb potential for each single scatterers,

$$U(\boldsymbol{r}) = \pm\frac{e^2}{\kappa r}\exp\left(-q_s r\right), \tag{2.53}$$

where κ is the static dielectric constant, and scatterers of $\pm$ are randomly distributed with equal probability, and q_s is the Thomas-Fermi screening constant given by

$$q_s^2 = \frac{4\pi e^2}{\kappa} D(\varepsilon_F), \tag{2.54}$$

at zero temperature. U is Fourier transformed as $U(\boldsymbol{r}) = \int \mathrm{d}\boldsymbol{q} u(\boldsymbol{q}) e^{i\boldsymbol{q}\cdot\boldsymbol{r}}/(2\pi)^3$ where

$$u(\boldsymbol{q}) = \pm\frac{4\pi e^2}{\kappa(q^2 + q_s^2)}. \tag{2.55}$$

We introduce an effective fine-structure constant

$$\alpha = \frac{e^2}{\kappa\hbar v}, \tag{2.56}$$

which characterizes the scattering strength. For the 3D Weyl electron in Cd_3As_2, for example, α is estimated at about 0.06 from $v \approx 1.0 \times 10^6 \mathrm{ms}^{-1}$ and $\kappa \approx 36$. [16, 15, 61, 62] We define a wave vector scale and an energy scale,

$$q_0 = n_i^{1/3}, \tag{2.57}$$

$$\varepsilon_0 = \hbar v q_0, \tag{2.58}$$

where n_i is the number of scatterers per unit volume.

2.2.1 Boltzmann transport theory

For the Coulomb impurities, the relaxation time is derived analytically and written as

$$\tau_{\rm tr}(\varepsilon) = \frac{\varepsilon^2}{4\pi\hbar^2 v^3 n_{\rm i}} h(\alpha), \tag{2.59}$$

where

$$h(\alpha) = \frac{1}{\alpha^2}\left[\left(1+\frac{\alpha}{\pi}\right)\tanh^{-1}\left(\frac{1}{1+\alpha/\pi}\right) - 1\right]^{-1}. \tag{2.60}$$

The conductivity at $T = 0$ is given by

$$\sigma_{\rm B}(\varepsilon) = e^2 \frac{v^2}{3} D_0(\varepsilon)\tau_{\rm tr}(\varepsilon), \tag{2.61}$$

and written as

$$\sigma_{\rm B}(\varepsilon) = \frac{1}{24\pi^3}\frac{e^2 q_0}{\hbar}\left(\frac{\varepsilon}{\varepsilon_0}\right)^4 h(\alpha). \tag{2.62}$$

Since the electron concentration n is proportional to $\varepsilon_{\rm F}^3$ in the 3D linear band, the Boltzmann conductivity $\sigma_{\rm B}$ is proportional to $n^{4/3}$. Figure 2.6 shows the conductivity Eq. (2.62) versus the Fermi energy $\varepsilon_{\rm F}$ for several values of α.

The Boltzmann conductivity in 3D Weyl electron was previously calculated under the conditon that the electron density is equal to the Coulomb impurity density, i.e., all carriers are supplied from the ionic impurities. [2] The result is reproduced by Eq. (2.62) with ε is replaced with $\hbar v(6\pi^2 n_{\rm i})^{1/3}$.

We see that the boltzmann conductivity away from the Weyl point is proportional to ε^4 in both potentials, while the boltzmann conductivity has a finite minimum conductivity in the Gaussian potential case but it vanishes at the Weyl point in the Coulomb potential case. This is because the Coulomb potential is not screened at the Weyl point.

2.2.2 Approximate analytical solution of SCBA

The formulation of SCBA in Sec. 2.1.2 also applies to the Coulomb potential case. Here we solve the SCBA equation approximately to get analytical expressions for the density of states and the conductivity at the Weyl point ($\varepsilon = 0$). In the following, we solve the self-consistent Eqs. (2.26) and (2.27) at $\varepsilon = 0$ using a certain approximation to simplify the problem. We first assume $Y(k, 0)$ is written as

$$Y(k, 0) = \hbar v k, \tag{2.63}$$

i.e., we neglect the Σ_2 term in Eq. (2.19). We can show that Σ_2 is also linear to k in the real solution, and thus it gives Fermi velocity renormalization, while it does not change the qualitative behavior of the density of states and the conductivity. Then the equation (2.26) for $X(k) = X(k, 0)$ is written as

$$X(k) = -\int_0^\infty \frac{k'^2 {\rm d}k'}{(2\pi)^3} n_{\rm i} V_0^2(k, k') \frac{X(k')}{(X(k'))^2 - (\hbar v k')^2}, \tag{2.64}$$

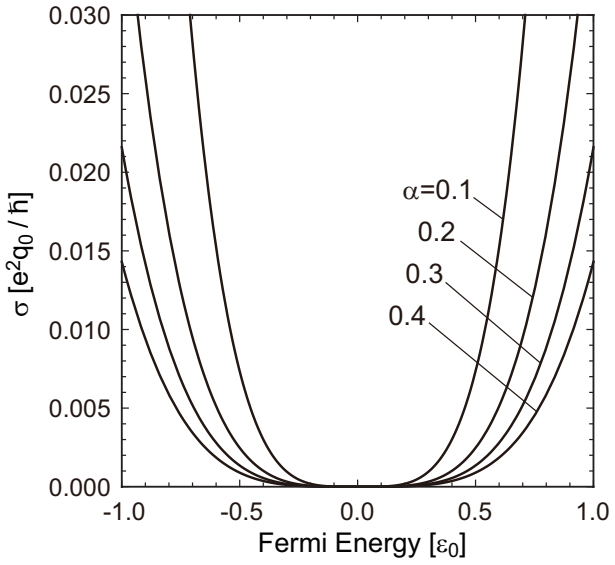

Figure 2.6: Boltzmann conductivity [Eq. (2.62)] plotted as a function of the Fermi energy.

where

$$V_0^2(k,k') = \left(\frac{4\pi e^2}{\kappa}\right)^2 \frac{4\pi}{(k^2+k'^2+q_{\rm s}^2)^2 - 4k^2k'^2}. \tag{2.65}$$

First we consider the solution $X(k)$ in $k \gg q_{\rm s}$. $V_0^2(k,k')$ can be approximately written by a delta function as

$$k'^2 V_0^2(k,k') \approx \left(\frac{4\pi e^2}{\kappa}\right)^2 \frac{\pi^2}{q_{\rm s}} \delta(k-k'), \tag{2.66}$$

and Eq. (2.64) then becomes

$$X(k) = -\frac{n_{\rm i}}{(2\pi)^3}\left(\frac{4\pi e^2}{\kappa}\right)^2 \frac{\pi^2}{q_{\rm s}} \frac{X(k)}{(X(k))^2 - (\hbar v k)^2}. \tag{2.67}$$

The physically plausible solution is

$$X(k) = \begin{cases} i\sqrt{\Gamma_0^2 - (\hbar v k)^2} & (k < \Gamma_0/(\hbar v)), \\ 0 & (k > \Gamma_0/(\hbar v)), \end{cases} \tag{2.68}$$

where

$$\Gamma_0 = \hbar v q_0 \sqrt{\frac{2\pi\alpha^2}{(q_{\rm s}/q_0)}}. \tag{2.69}$$

Therefore, $X(k)$ attenuates with the increase of k and vanishes at $k = \Gamma_0/(\hbar v)$.

For $k = 0$, we need a special treatment since the approximation Eq. (2.66) is not valid in $k < q_{\rm s}$. The self-consistent equation at $k = 0$ is written as

$$X(0) = -\int_0^\infty \frac{k'^2 {\rm d}k'}{(2\pi)^3} n_{\rm i} \left(\frac{4\pi e^2}{\kappa}\right)^2 \frac{4\pi}{(k'^2 + q_{\rm s}^2)^2} \times \frac{X(k')}{(X(k'))^2 - (\hbar v k')^2}. \tag{2.70}$$

On the condition that $\Gamma_0 \gg \hbar v q_{\rm s}$, the term $(k'^2 + q_{\rm s}^2)^{-2}$ is a rapidly changing function compared to $X(k')$, and it vanishes except in the vicinity of $k' = 0$. Then $X(k')$ can be replaced by $X(0)$ in the integral, and we obtain a solution,

$$X(0) = i\Gamma, \tag{2.71}$$

with

$$\Gamma = \Gamma_0 - \hbar v q_{\rm s}. \tag{2.72}$$

When compared to Eq. (2.68), we notice that $X(0)$ has an additional correction term $-i\hbar v q_{\rm s}$, which is actually important in considering the limit of $\alpha \to 0$. All the approximation above is based on the assumption $\Gamma_0 \gg \hbar v q_{\rm s}$, and this is actually satisfied in the situation considered in the later sections.

Based on the above arguments, we introduce a crude approximation by even simplifying $X(k)$ to a step function as

$$X(k) = \begin{cases} i\Gamma & (k < \Gamma/(\hbar v)) \\ 0 & (k > \Gamma/(\hbar v)) \end{cases}, \tag{2.73}$$

with Γ defined in Eq. (2.72). Substituting Eq. (2.63) and (2.73) for Eq. (2.28), we find the density of states

$$D(\varepsilon = 0) = \frac{\Gamma^2}{(\hbar v)^3} \frac{f}{4\pi}, \tag{2.74}$$

$$f = \frac{4 - \pi}{\pi^2} \approx 0.087, \tag{2.75}$$

and from Eq. (2.54), the screening constant is written as

$$q_{\rm s} = \frac{\Gamma}{\hbar v} \sqrt{f\alpha}. \tag{2.76}$$

By solving Eq. (2.72) and (2.76), we have

$$\Gamma = \varepsilon_0 \left(\frac{2\pi}{\sqrt{f}(1 + \sqrt{f\alpha})^2}\right)^{1/3} \sqrt{\alpha}. \tag{2.77}$$

In $\alpha \ll 1$, Γ is nearly proportional to $\sqrt{\alpha}$ and the density of states is proportional to Γ^2, thus to α.

The Bethe-Salpeter equation Eq. (2.35) can be approximately solved at $\varepsilon = 0$ in a similar manner. We assume the form of the solution as,

$$\begin{pmatrix} J_0^{+s}(k) \\ J_1^{+s}(k) \\ J_2^{+s}(k) \\ J_3^{+s}(k) \end{pmatrix} \approx \begin{pmatrix} J_0^{+s}(k) \\ 0 \\ 0 \\ 0 \end{pmatrix}, \tag{2.78}$$

where $s = \pm$. Then the equation is reduced to

$$\begin{aligned} J_0^{+s}(k) = 1 + \int_0^\infty \frac{k'^2 \mathrm{d}k'}{(2\pi)^3} \frac{n_\mathrm{i}}{(X^2 - Y^2)(X'^2 - Y'^2)} \\ \times \left(V_0^2 X X' - \frac{V_0^2 - V_2^2}{2} Y Y' \right) J_0^{+s}(k'). \end{aligned} \tag{2.79}$$

In a similar manner to $X(k)$, we find a solution,

$$J_0^{+s}(k) = \begin{cases} J^{+s} & (k < \Gamma/(\hbar v)) \\ 0 & (k > \Gamma/(\hbar v)) \end{cases}, \tag{2.80}$$

where

$$J^{+s} = \left[1 + s \frac{2\pi\alpha^2 (3q_\Gamma - q_\mathrm{s}) q_0^3}{3q_\mathrm{s}(q_\Gamma + q_\mathrm{s})^3} \right]^{-1}, \tag{2.81}$$

and $q_\Gamma = \Gamma/(\hbar v)$. In $\alpha \ll 1$, J^{+s} can be expanded in the lowest order of α as

$$J^{+-} \approx \frac{3}{4\sqrt{f}} \frac{1}{\sqrt{\alpha}}, \quad J^{++} \approx \frac{1}{2}, \tag{2.82}$$

i.e., J^{+-} diverges in $\alpha \to 0$ while J^{++} remains constant. In small α, therefore, we can neglect J_0^{++} in Eq. (2.36) leaving only J_0^{+-}, and then the conductivity is calculated as

$$\begin{aligned} \sigma(\varepsilon = 0) \approx & \frac{4\hbar e^2 v^2}{3} \int_0^{\Gamma/(\hbar v)} \frac{k^2 \mathrm{d}k}{(2\pi)^3} \frac{3J^{+-}}{\Gamma^2} \\ = & \frac{J^{+-}}{6\pi^3} \frac{e^2}{\hbar} \frac{\Gamma}{\hbar v}. \end{aligned} \tag{2.83}$$

Using Eq. (2.82), the conductivity in the limit of $\alpha \to 0$ becomes

$$\begin{aligned} \sigma(\varepsilon = 0) &\approx \frac{1}{8\pi^3} \left(\frac{2\pi}{f^2} \right)^{1/3} \frac{e^2 q_0}{\hbar} \\ &\approx 0.038 \times \frac{e^2 q_0}{\hbar}. \end{aligned} \tag{2.84}$$

Here the magnitude of the conductivity is determined solely by the impurity density $n_\mathrm{i} = q_0^3$, and it scales in proportion to $n_\mathrm{i}^{1/3}$.

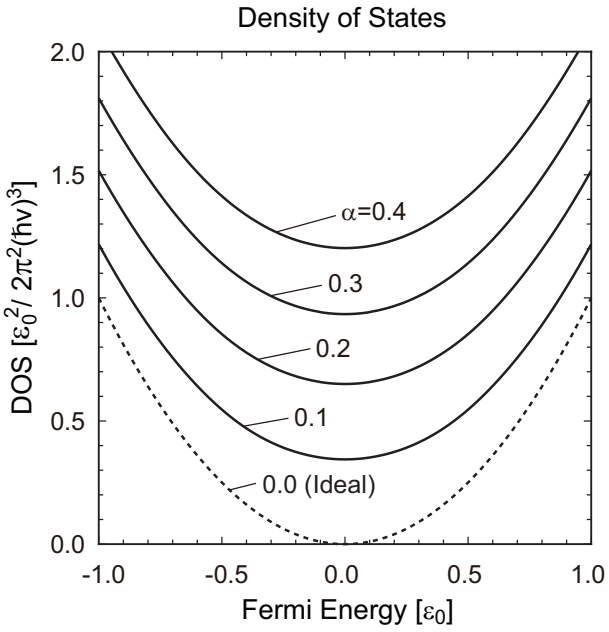

Figure 2.7: Density of states calculated by the SCBA, as a function of the Fermi energy at several values of α.

The conductivity formula Eq. (2.83) is almost equivalent to the analytical expression for the Gaussian impurities [40], but the actual behavior of the conductivity is significantly different. In the Gaussian case, the vertex part J^{+-} is constant and the level broadening Γ vanishes below the critical disorder strength. As a result, the conductivity vanishes in the weak disorder regime. In the Coulomb impurity case, on the other hand, J^{+-} diverges as $1/\sqrt{\alpha}$ in the limit of $\alpha \to 0$, while the level broadening vanishes as $\sqrt{\alpha}$. Therefore, $J^{+-}\Gamma$ approaches constant, giving a finite minimum conductivity in the limit of $\alpha \to 0$.

A finite conductivity at absolutely no scattering ($\alpha = 0$) looks counterintuitive, but here we should note that the result is based on the implicit assumption that the transport is diffusive, i.e. the system size is much greater than the mean free path. If we take a limit $\alpha \to 0$ in a fixed-sized system, the mean free path exceeds the system size at some point and then the diffusive transport switches to the ballistic transport, to which the present conductivity formula does not apply.

2.2.3 Numerical solution of SCBA

Figure 2.7 shows the density of states as a function of the Fermi energy at several values of α. The density of states is enhanced in all energy region linearly to α, and this is consistent with the behavior in the analytical expression at $\varepsilon = 0$ in the previous section [Eqs. (2.74) and (2.77)]. Fig. 2.9(a) shows the level broadening $\Gamma = \mathrm{Im}[X(k = 0, \varepsilon = 0)]$ as a function of α, where the solid line shows the numerical result and the dashed line shows the approximate solution Eq. (2.77). Fig. 2.9(b) is a similar plot for the density of states $D(\varepsilon = 0)$ as a function of α, where the solid line represent the numerical result and

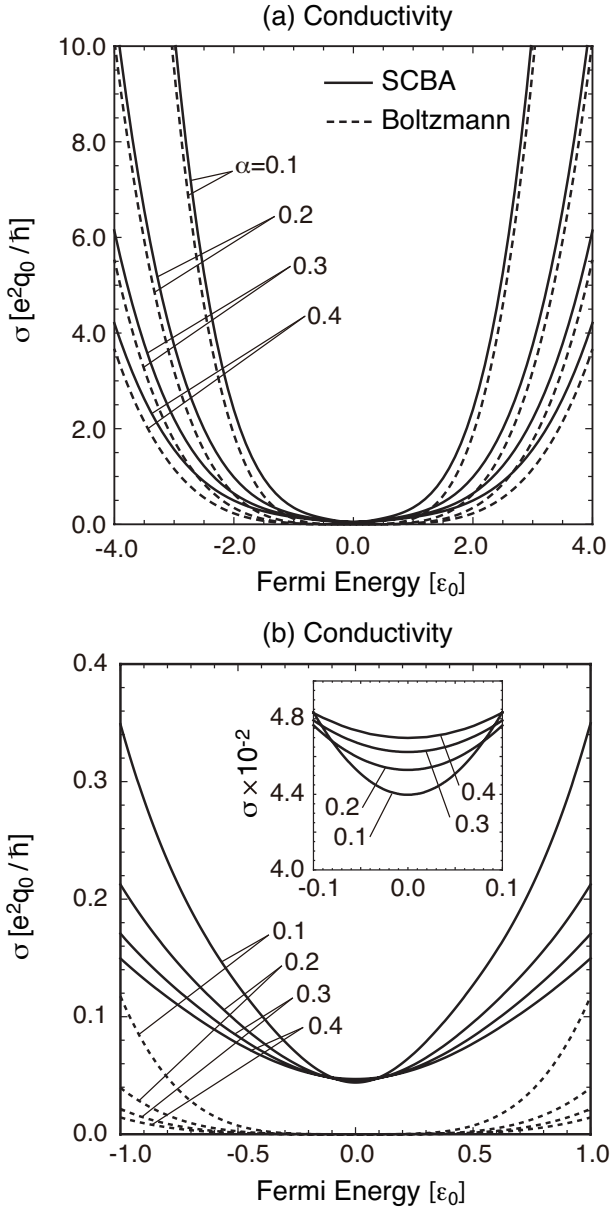

Figure 2.8: Conductivity as a function of the Fermi energy in different plot ranges. In each panel, the solid lines represent the SCBA and the dashed lines represent the Boltzmann theory. The inset in (b) shows the detailed plot for the SCBA conductivity around the Weyl point.

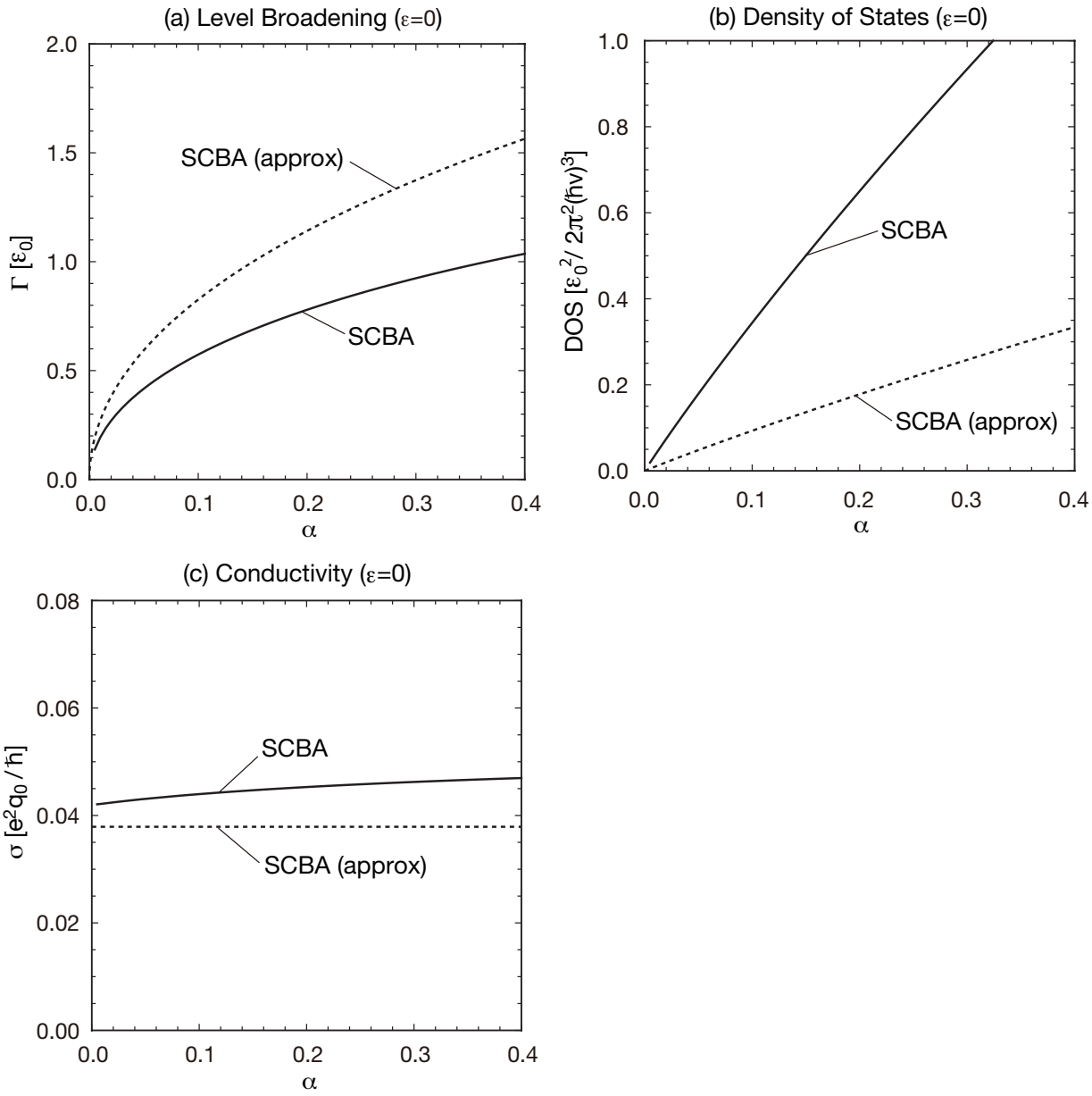

Figure 2.9: Density of states and the conductivity as a function of α. The solid line represent the numerical result and the dashed line represent the approximate analytical expression (see text).

the dashed line represent the approximate analytical expression Eq. (2.74). We see that in the both plots the analytical expression well reproduces the qualitative behavior of the numerical result, i.e., $\Gamma \propto \sqrt{\alpha}$ and $D(0) \propto \alpha$.

Figs. 2.8(a) and (b) shows the conductivity as a function of the Fermi energy for several values of α. In Fig. 2.8(a), we see that the SCBA result mostly agrees with the Boltzmann theory away from $\varepsilon = 0$, where the conductivity is proportional to ε^4 and increases with the decrease of α as expected from Eq. (2.62). Fig. 2.8(b) shows the detailed plot around the Weyl point. Now we see a considerable disagreement between the two results, where the Boltzmann conductivity vanishes at the Weyl point, although the SCBA conductivity has a finite value. The Boltzmann theory is valid when the Fermi energy is much greater than the level broadening Γ, so that the energy region where the Boltzmann theory fails becomes wider with the increase of α. We actually see this behavior in Figs. 2.8(a).

Fig. 2.9(c) shows the zero-energy conductivity $\sigma(0)$ as a function of α, where the solid line indicates the numerical result and the dashed line the analytical expression Eq. (2.84). The numerical curve is nearly constant depending on α only weakly. In the limit of $\alpha \to 0$, it actually approaches a finite value, and the magnitude agrees qualitatively well with the analytic estimation of Eq. (2.84).

2.3 Discussion

2.3.1 Validity of SCBA at the Weyl point

Since the SCBA only partially takes the self-enegy diagrams in the perturbational expansion, it is generally suppose to be valid when the scattering strength is relatively weak. Fig. 2.10 (a) expresses SCBA self-energy $\Sigma_{\rm SCBA}$, and (b) shows the leading correction term $\Sigma_{\rm corr}$ which was neglected in the SCBA. The SCBA is qualitatively correct when $\Sigma_{\rm corr}$ is much smaller than $\Sigma_{\rm SCBA}$. In the conventional disordered metal, we have $\Sigma_{\rm corr}/\Sigma_{\rm SCBA} = \mathcal{O}(1/k_{\rm F}l)$ with the Fermi wave vector $k_{\rm F}$ and the mean free path l.

It is nontrivial if the SCBA is valid at the Weyl point where $k_{\rm F}$ becomes zero.[63, 64] In the presence of the disorder potential, $k_{\rm F}$ does not actually vanish but it is effectively replaced with $\sim \Gamma/(\hbar v)$ due to the finite level broadening Γ. Meanwhile the mean free path l is given by $v\tau$ where v is the constant band velocity and $\tau = \hbar/\Gamma$ is the scattering time. Then we end up with $k_F l = \mathcal{O}(1)$, which means the correction term is not actually negligible.

In a recent theoretical study [64], the conductivity in the single-node 3D Weyl electron is numerically calculated in the presence of the Gaussian impurities using the Landuer formulation. The behaviors of the Weyl-point self-energy and conductivity are found to be consistent with the corresponding SCBA calculation [40], while there is a quantitative discrepancy by a factor. Ref.[64] also estimated the leading correction term $\Sigma_{\rm corr}$ in the numerical calculation and it was found to be smaller than $\Sigma_{\rm SCBA}$ but not negligibly small. This is actually responsible for the quantitative descrepancy in the SCBA.

In the following, we consider the extended SCBA approximation including the leading correction term $\Sigma_{\rm corr}$ for the screened Coulomb impurity case, and show that the additonal term does not change the qualitative behevior of the total self-energy. The extended self-

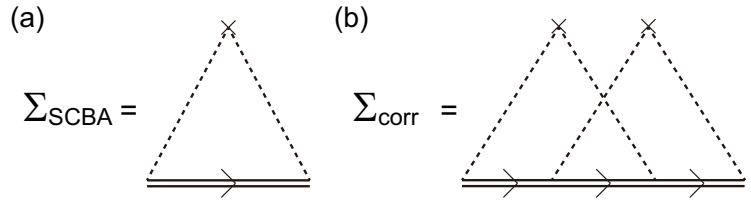

Figure 2.10: The diagrammatic representations of (a) the self-energy for the SCBA and (b) the leading correction term for the SCBA.

consistent equation including the diagrams of Fig. 2.10 (a) and (b) is written as

$$\begin{aligned}\hat{\Sigma}(\boldsymbol{k},\varepsilon) = &\int \frac{\mathrm{d}\boldsymbol{k}'}{(2\pi)^3} n_{\mathrm{i}} |u(\boldsymbol{k}-\boldsymbol{k}')|^2 \hat{G}(\boldsymbol{k}',\varepsilon) \\ &+ \int \frac{\mathrm{d}\boldsymbol{k}'}{(2\pi)^3} \int \frac{\mathrm{d}\boldsymbol{k}''}{(2\pi)^3} n_{\mathrm{i}}^2 |u(\boldsymbol{k}-\boldsymbol{k}')|^2 |u(\boldsymbol{k}'-\boldsymbol{k}'')|^2 \\ &\quad \times \hat{G}(\boldsymbol{k}',\varepsilon)\hat{G}(\boldsymbol{k}'',\varepsilon)\hat{G}(\boldsymbol{k}-\boldsymbol{k}'+\boldsymbol{k}'',\varepsilon). \end{aligned} \tag{2.85}$$

We consider the Weyl point $\varepsilon = 0$ and assume $\hat{\Sigma} = -i\Gamma$ and $q_{\mathrm{s}} \ll \Gamma/(\hbar v)$ as done in Sec. 2.2.2. As the $u(\boldsymbol{k})$ term is relevant only when $k <\sim q_s$, we can replace the Green's function $\hat{G}(\boldsymbol{k})$ with $1/(i\Gamma)$ under the present assumption $k <\sim q_{\mathrm{s}} \ll \Gamma/(\hbar v)$. Then k-integral simply gives I of Eq. (2.93), and the self-consistent equation (2.85) is reduced to

$$\Gamma = \Gamma \left[\left(\frac{\Gamma_0}{\Gamma} \right)^2 + \left(\frac{\Gamma_0}{\Gamma} \right)^4 \right], \tag{2.86}$$

where Γ_0 is defined in Eq. (2.69). By solving this, we find a non-trivial solution

$$\Gamma = \sqrt{\frac{1+\sqrt{5}}{2}}\Gamma_0. \tag{2.87}$$

The ratio of the second term to the first term in Eq. (2.86) then gives

$$\frac{\Sigma_{\mathrm{corr}}}{\Sigma_{\mathrm{SCBA}}} = \left(\frac{\Gamma_0}{\Gamma} \right)^2 = \frac{-1+\sqrt{5}}{2} \approx 0.618\cdots, \tag{2.88}$$

i.e., Σ_{corr} is smaller than Σ_{SCBA} while not negligibly small. In fact, Eq. (2.88) is close to the value numerical estimated for the Gaussian impurity case in Ref. [64].

In the usual SCBA approach without Σ_{corr} in the previous section, we only take the first term in the bracket of Eq. (2.86) and obtain $\Gamma = \Gamma_0$. Comparing to Eq. (2.87), we see that the correction term attaches a numerical factor in front of the SCBA self-energy. Therefore, we expect that adding the correction terms does not change the qualitative behavior of the total self-energy.

2.3.2 Critical behavior in a general impurity potential under the screening effect

We can show that the critical behavior observed in the Gaussian potential is never observed in the bare (i.e., unscreened) Coulomb potential, and the absence of the critical point is attributed to the divergence of $u(q)$ in the limit of $q \to 0$.[40]

Unlike the bare Coulomb potential, the screened Coulomb potential studied in this paper does not diverge in $q \to 0$ due to the finite screening length, and then we naively expect the critical behavior takes place in a similar way to Gaussian impurities. Contrary to such an expectation, the detailed calculation in the above section showed no critical behaviors in the screened Coulomb impurity. To resolve this apparent discrepancy, we argue in the following about the criteria for the critical behavior in general impurity potential with the screening effect.

We consider the isotropic impurity potential $U(r)$ (and its Fourier tranform $u(k)$), and assume an approximate solution for the self-consistent equation,

$$X(k,0) = i\Gamma, \tag{2.89}$$

$$Y(k,0) = \hbar v k. \tag{2.90}$$

Then Eq. (2.67) at $k = 0$ is written as

$$\Gamma = \frac{n_{\rm i}}{2\pi^2} \int_0^\infty k'^2 {\rm d}k' u(k')^2 \frac{\Gamma}{\Gamma^2 + (\hbar v k')^2}. \tag{2.91}$$

Obviously, Eq. (2.91) has a trivial solution $\Gamma = 0$, and another solution is obtained from

$$1 = \frac{n_{\rm i}}{2\pi^2} \int_0^\infty k'^2 {\rm d}k' u(k')^2 \frac{1}{\Gamma^2 + (\hbar v k')^2}. \tag{2.92}$$

When the right-hand side of Eq. (2.92) is viewed as a function of Γ, it takes the maximum value at $\Gamma = 0$, which is written as,

$$I = \frac{n_{\rm i}}{2\pi^2 \hbar^2 v^2} \int_0^\infty {\rm d}k' u(k')^2. \tag{2.93}$$

When I is smaller than 1, Eq. (2.92) cannot be satisfied by any Γ, and then $\Gamma = 0$ is the only solution of Eq. (2.91). In the case of the Gaussian potential $u(k) = u_0 \exp(-k^2/k_0^2)$, for example, the integral I becomes a finite value proportional to $n_{\rm i} u_0^2$, and Γ (and thus the density of states) vanishes when $n_{\rm i} u_0^2$ is lower than a certain critical value. [40]

For the screened Coulomb potential, i.e., $u(k) = (4\pi e^2/\kappa)/(k'^2 + q_{\rm s}^2)$, we have

$$I = 2\pi\alpha^2 \left(\frac{q_0}{q_{\rm s}}\right)^3, \tag{2.94}$$

and the condition for having only a trivial solution $\Gamma = 0$ is

$$1 \geq 2\pi\alpha^2 \left(\frac{q_0}{q_{\rm s}}\right)^3. \tag{2.95}$$

If we treat $q_{\rm s}$ as a constant, Eq. (2.95) is satisfied when α is sufficiently small. However, α and $q_{\rm s}$ are not actually independent in the self-consistent calculation, as we argued in Sec. 2.2.2. Using the self-consistent solution Eqs. (2.76) and (2.77), Eq. (2.95) is rewritten as

$$1 \geq \left(1 + \frac{1}{\sqrt{f\alpha}}\right)^2, \tag{2.96}$$

which cannot be true. In a screened Coulomb scatterers, therefore, we always have a nonzero solution for Γ and there is no critical disorder scattering strength.

On the other hand, we can show that the critical disorder strength does exist in Gaussian scatterers even when including the screening effect, which was neglected in the previous Section. The screened Gaussian potential is written as

$$u(k) = \frac{u_0 \exp(-k^2/k_0^2)}{1 + q_{\rm s}^2/k^2}, \tag{2.97}$$

giving

$$I = \frac{n_{\rm i} u_0^2}{2\pi^2 \hbar^2 v^2} \int_0^\infty {\rm d}k' \left(\frac{\exp(-k'^2/k_0^2)}{1 + q_{\rm s}^2/k'^2}\right)^2. \tag{2.98}$$

The inverse screening length $q_{\rm s}$ is to be self-consistently determined by Eq. (2.54). Unlike the Coulomb impurity [Eq. (2.94)], the intergral I never diverges in any value of $q_{\rm s}$ and it has an upper bound $I_{\rm max}$ at $q_{\rm s} = 0$. In a sufficiently small $n_{\rm i} u_0^2$ such that $I_{\rm max} < 1$, therefore, we have only a trivial solution $\Gamma = 0$ regardless of $q_{\rm s}$, while this is a sufficient but not necessary condition.

Following the above discussion, we see that whether a critical disorder strength exists depends on the specific form of the impurity potential, even when the screening effect is included. We can examine the existence of the critical disorder strength for any type of impurity scatterers in a similar way, by estimating the maximum value of the intergral I in Eq. (2.93) as a function of $q_{\rm s}$.

Chapter 3

Magnetotransport in the Weyl semimetal

In this chapter, we study the magnetotransport property of a Weyl semimetal having the surface boundary, to investigate the effect of the topological surface states on the giant positive magnetoconductivity. Here we consider the tight-binding lattice model having a pair of point nodes around which the band structure is approximately described by the Weyl Hamiltonian. We consider a surface boundary where the surface state bands connect the two Weyl cones as shown in Fig. 1.4. When a magnetic field **B** is applied in parallel to the surface, we find that the surface band is seamlessly connected to the 0-th Landau level of the bulk spectrum, and form a closed Fermi surface. For this situation, we calculate the conductivity of the system under the electric field **E** parallel to **B**, using the Boltzmann transport theory. We find that the conductivity behavior becomes completely different from that of the infinite system, where the surface states play a crucial role in the relaxation of the bulk carriers.

3.1 Formulation

3.1.1 Lattice model

We consider a tight-binding model on a cubic lattice. The nearest-neighbor hopping term is schematically represented in Fig. 3.1. Each lattice site on a coordinate (x, y, z) is represented as (n_x, n_y, n_z) with integer n_x, n_y, n_z. The wave function is written as

$$|\psi\rangle = \sum_{n_x,n_y,n_z} \overrightarrow{\psi}(x, y, z)|n_x, n_y, n_z\rangle, \tag{3.1}$$

where $|n_x, n_y, n_z\rangle$ is a localized state on a site (n_x, n_y, n_z), and $\overrightarrow{\psi}(x, y, z)$ is a two component vector. The Hamiltonian is written as

$$H = 2t\left(\sigma_x \sin k_x a + \sigma_y \sin k_y a + \sigma_z \cos k_z a\right) + 2m\sigma_z(2 - \cos k_x a - \cos k_y a), \tag{3.2}$$

where σ_i $(i = x, y, z)$ are the Pauli matrices, and a is a lattice constant. We set $m = t$ in the following calculation. In the real space, the Schrödinger equation becomes

$$\begin{aligned}(\varepsilon/t)\overrightarrow{\psi}(x,y,z) =&(-i\sigma_x - \sigma_z)\overrightarrow{\psi}(x+a,y,z) + (i\sigma_x - \sigma_z)\overrightarrow{\psi}(x-a,y,z)\\ &+(i\sigma_y - \sigma_z)\overrightarrow{\psi}(x,y+a,z) + (-i\sigma_y - \sigma_z)\overrightarrow{\psi}(x,y-a,z)\\ &+\sigma_z\left[\overrightarrow{\psi}(x,y,z+a) + \overrightarrow{\psi}(x,y,z-a) + 4\overrightarrow{\psi}(x,y,z)\right]. \end{aligned} \tag{3.3}$$

We consider electronic states in the presence of a magnetic field parallel to z axis. We take Landau gauge and set the vector potential as

$$\boldsymbol{A} = (-By, 0, 0). \tag{3.4}$$

The eigenstate is written as

$$\begin{aligned}|n, \boldsymbol{k}\rangle &= \sum_{n_x,n_y,n_z} \overrightarrow{\psi}_{n\boldsymbol{k}}(x,y,z)|n_x,n_y,n_z\rangle,\\ \overrightarrow{\psi}_{n\boldsymbol{k}}(x,y,z) &= \frac{1}{\sqrt{N_x N_z}} e^{i(k_x x + k_z z)}\overrightarrow{\phi}_{n\boldsymbol{k}}(y),\end{aligned} \tag{3.5}$$

where n is a band index, and $\boldsymbol{k} = (k_x, k_z)$ is a wave vector on a x-z plane. The Schrödinger equation becomes

$$\begin{aligned}(\varepsilon/t)\overrightarrow{\phi}_{n\boldsymbol{k}}(y) =&(-i\sigma_x - \sigma_z)e^{ik_x a}e^{ieBya/\hbar}\overrightarrow{\phi}_{n\boldsymbol{k}}(y)\\ &+(i\sigma_x - \sigma_z)e^{-ik_x a}e^{-ieBya/\hbar}\overrightarrow{\phi}_{n\boldsymbol{k}}(y)\\ &+(i\sigma_y - \sigma_z)\overrightarrow{\phi}_{n\boldsymbol{k}}(y+a) + (-i\sigma_y - \sigma_z)\overrightarrow{\phi}_{n\boldsymbol{k}}(y-a)\\ &+\sigma_z(4 + e^{ik_z a} + e^{-ik_z a})\overrightarrow{\phi}_{n\boldsymbol{k}}(y),\end{aligned} \tag{3.6}$$

and this is written as

$$\begin{aligned}(\varepsilon/t)\overrightarrow{\phi}_{n\boldsymbol{k}}(y) =&2\sin(k_x a + 2\pi\phi y/a)\sigma_x\overrightarrow{\phi}_{n\boldsymbol{k}}(y)\\ &+\left[4 - 2\cos(k_x a + 2\pi\phi y/a) + 2\cos(k_z a)\right]\sigma_z\overrightarrow{\phi}_{n\boldsymbol{k}}(y)\\ &+(i\sigma_y - \sigma_z)\overrightarrow{\phi}_{n\boldsymbol{k}}(y+a) + (-i\sigma_y - \sigma_z)\overrightarrow{\phi}_{n\boldsymbol{k}}(y-a),\end{aligned} \tag{3.7}$$

where $\phi = Ba^2/(h/e)$. Solving Eq. (3.7), we obtain the band structure.

Fig. 3.2 (a) presents the bulk band structure in the zero magnetic field. The two bands are touching at the Weyl points located at $k_z = \pm k_0$ where $k_0 = \pm\pi/(2a)$. Fig. 3.2(b) presents the spectrum under a finite magnetic field, where we see the Landau levels dispersing only in k_z direction (parallel to B).

Fig. 3.3 presents the band structure of the surface-bound system ($N_y = 20$) as a function of (k_x, k_z). The panel (a) is for the zero magnetic field ($\phi = 0$) and (b) is for the finite magnetic field $\phi = 0.003$. In (a), we see that the two Weyl cones are quantized into subbands due to the finite dimension in y, and they are bridged by the surface band. In the presence of the magnetic field [panel (b)], on the other hand, the lower surface band

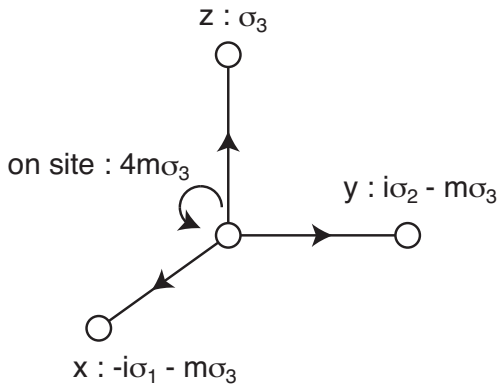

Figure 3.1: Schematic representation of the lattice model.

shifts upward in the energy axis. The equi-energy contour of $\varepsilon = 0$ becomes a rectangular-like shape. Significantly, the two sides along k_z are composed of the surface states while the other two sides along k_x are from the 0-th Landau levels of the bulk. So the bulk states and the surface states are seamlessly connected on a single Fermi surface.

Figure 3.4 is the zero-energy Fermi surfaces of different magnetic fields $\phi = 0.003, 0.006$ and 0.009. We see that the rectangular Fermi surface expands in k_x direction in increasing magnetic field, because of the increase of the Landau level degeneracy. The surface state part remains almost unchanged.

3.1.2 Boltzmann transport theory

Boltzmann transport equation is given by

$$\frac{\partial f_{\boldsymbol{k}}}{\partial t} = \frac{e}{\hbar}\boldsymbol{E}\cdot\frac{\partial f_{\boldsymbol{k}}}{\partial \boldsymbol{k}} + \left(\frac{\partial f_{\boldsymbol{k}}}{\partial t}\right)_{\text{coll}}, \tag{3.8}$$

where

$$\left(\frac{\partial f_{\boldsymbol{k}}}{\partial t}\right)_{\text{coll}} = \sum_{\boldsymbol{k}'}\left[f_{\boldsymbol{k}'}(1-f_{\boldsymbol{k}})W_{\boldsymbol{k}\boldsymbol{k}'} - f_{\boldsymbol{k}}(1-f_{\boldsymbol{k}'})W_{\boldsymbol{k}'\boldsymbol{k}}\right],$$
$$W_{\boldsymbol{k}\boldsymbol{k}'} = \frac{2\pi}{\hbar}\langle|V_{\boldsymbol{k}\boldsymbol{k}'}|^2\rangle\delta(\varepsilon_{\boldsymbol{k}}-\varepsilon_{\boldsymbol{k}'}), \tag{3.9}$$

and $f_{\boldsymbol{k}}$ is a Fermi distribution function.

We define $g_{\boldsymbol{k}}$ as

$$f_{\boldsymbol{k}} = f^0_{\boldsymbol{k}} + g_{\boldsymbol{k}}, \tag{3.10}$$

and in the presence of the electric field in the z-direction, Eq. (3.8) is written as

$$\frac{e}{\hbar}E_z v_{\boldsymbol{k}z}\left(-\frac{\partial f^0(\varepsilon)}{\partial\varepsilon}\right)_{\varepsilon=\varepsilon_{\boldsymbol{k}}} = \sum_{\boldsymbol{k}'}\left(g_{\boldsymbol{k}'}-g_{\boldsymbol{k}}\right)W_{\boldsymbol{k}\boldsymbol{k}'}. \tag{3.11}$$

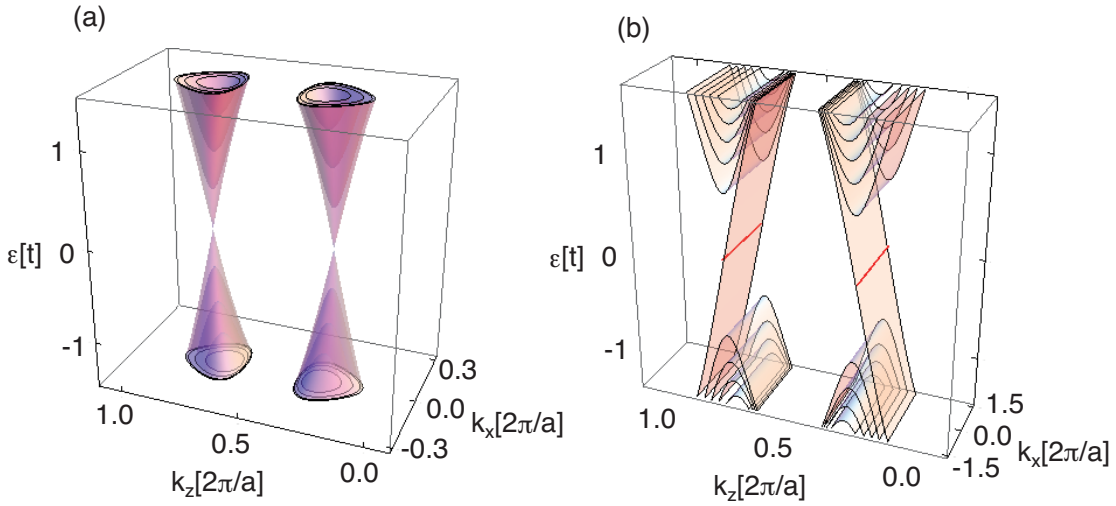

Figure 3.2: Energy band structures of the bulk system near $\varepsilon = 0$, in the absence of magnetic field (a), and in the presence of magnetic field (b).

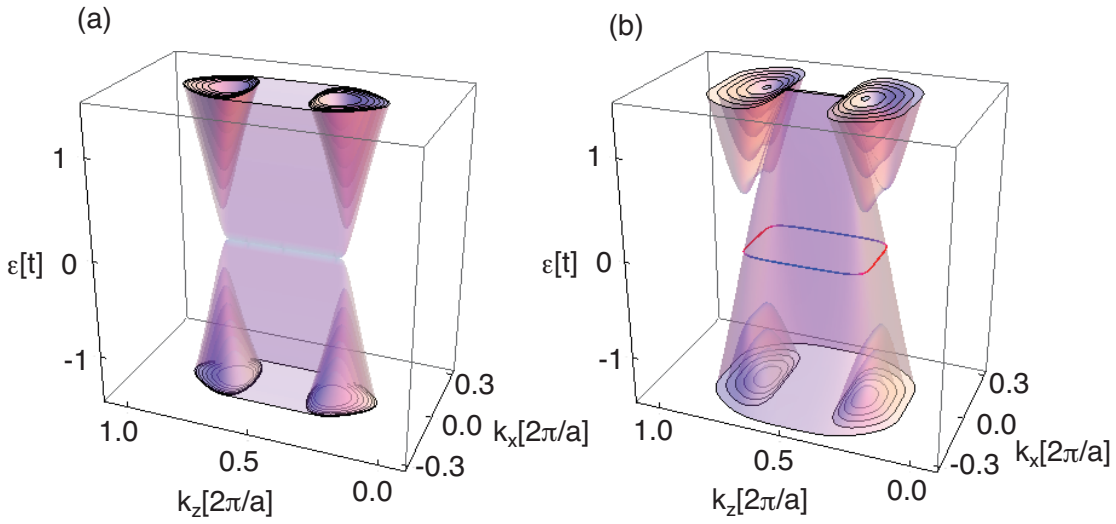

Figure 3.3: Energy band structures of the surface-bound system for $N_y = 30$ near $\varepsilon = 0$. (a) $\phi = 0.00$. (b) $\phi = 0.01$.

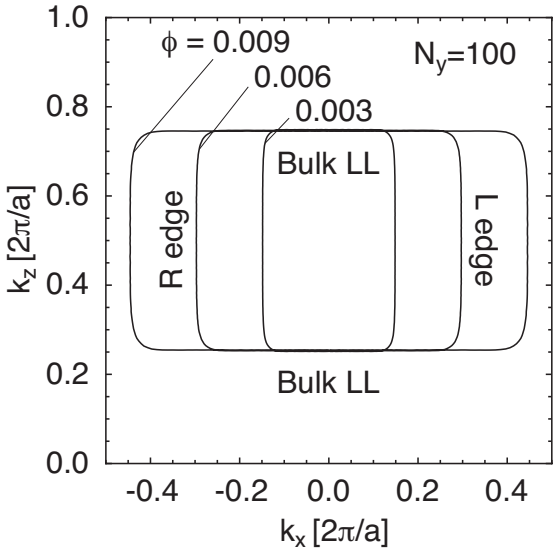

Figure 3.4: Fermi surface for $N_y = 100$ and $\phi = 0.003, 0.006, 0.009$.

We define $h_{\boldsymbol{k}}$ and a relaxation time $\tau_{\boldsymbol{k}}$ as

$$g_{\boldsymbol{k}} = (-e)E_z\tau_{\boldsymbol{k}}h_{\boldsymbol{k}}\left(-\frac{\partial f^0(\varepsilon)}{\partial\varepsilon}\right)_{\varepsilon=\varepsilon_{\boldsymbol{k}}}, \tag{3.12}$$

$$\frac{1}{\tau_{\boldsymbol{k}}} = \sum_{\boldsymbol{k}'} W_{\boldsymbol{k}\boldsymbol{k}'}, \tag{3.13}$$

$$W_{\boldsymbol{k}\boldsymbol{k}'} = \frac{2\pi}{\hbar}\langle|V_{\boldsymbol{k}\boldsymbol{k}'}|^2\rangle\delta(\varepsilon_{\boldsymbol{k}} - \varepsilon'_{\boldsymbol{k}}), \tag{3.14}$$

where $\langle\cdots\rangle$ represents the average over the configuration of the impurity position, and then the Boltzmann equation becomes

$$h_{\boldsymbol{k}} = v_{\boldsymbol{k}z} + \sum_{\boldsymbol{k}'}\tau_{\boldsymbol{k}'}h_{\boldsymbol{k}'}W_{\boldsymbol{k}\boldsymbol{k}'}. \tag{3.15}$$

Solving this self-consistent equation, we obtain $g_{\boldsymbol{k}}$.

Here, we introduce the model scatterers for the impurity potential. We consider the Gaussian scatterers

$$\begin{aligned} U(\boldsymbol{r}) &= \frac{u_0}{c(d_0)^3}\exp\left(-\frac{r^2}{d_0^2}\right), \\ &= u_0u(x)u(y)u(z), \end{aligned} \tag{3.16}$$

where the normalization constant $c(d_0)$ and $u(x)$ are defined as

$$u(x) = \frac{1}{c(d_0)}\exp\left(-\frac{x^2}{d_0^2}\right), \tag{3.17}$$

$$c(d_0) = \sum_{n=-\infty}^{\infty} a\exp\left[-\frac{(na)^2}{d_0^2}\right], \tag{3.18}$$

so that the summation of the single impurity potential over all the lattice points becomes u_0/a^3. The impurity potential is given by

$$V(\boldsymbol{r}) = \sum_i U(\boldsymbol{r} - \boldsymbol{r}_i), \tag{3.19}$$

where $\boldsymbol{r}_i$ is the impurity position in the lattice. We define the volume density of the scatterers as n_i.

The impurity averaged matrix element, $\langle |V_{\boldsymbol{k}\boldsymbol{k}'}|^2 \rangle$, is calculated as

$$\langle |V_{\boldsymbol{k}\boldsymbol{k}'}|^2 \rangle = \frac{n_i u_0^2}{L_x L_z} \frac{c(d_0/\sqrt{2})}{c(d_0)^2} \tilde{u}^2(q_x)\tilde{u}^2(q_z) S_{\boldsymbol{k}\boldsymbol{k}'}, \tag{3.20}$$

where

$$\tilde{u}(q) = \exp\left[-\frac{(d_0 q)^2}{4}\right], \tag{3.21}$$

$$S_{\boldsymbol{k}\boldsymbol{k}'} = \sum_{n_y} \overrightarrow{\phi}^\dagger_{\boldsymbol{k}}(y) \overrightarrow{\phi}_{\boldsymbol{k}'}(y) \sum_{n_y'} \overrightarrow{\phi}^\dagger_{\boldsymbol{k}'}(y') \overrightarrow{\phi}_{\boldsymbol{k}}(y') \exp\left[-\frac{(y-y')^2}{2d_0^2}\right]. \tag{3.22}$$

The electric current density in the z-direction j_z is derived by

$$j_z = (-e)\frac{1}{V}\sum_{\boldsymbol{k}} v_{\boldsymbol{k}z} f_{\boldsymbol{k}}, \tag{3.23}$$

with the system volume V, and this becomes

$$j_z = \sigma_{zz} E_z, \tag{3.24}$$

where the magnetoconductivity σ_{zz} is derived by

$$\sigma_{zz} = \frac{e^2}{L_y}\frac{1}{(2\pi)^2}\int \mathrm{d}\boldsymbol{k} v_{\boldsymbol{k}z}\tau_{\boldsymbol{k}} h_{\boldsymbol{k}} \delta(\varepsilon_\mathrm{F} - \varepsilon_{\boldsymbol{k}}). \tag{3.25}$$

3.2 Conductivity of the infinite system

First, we calculate the conductivity in the absence of edge, i.e. the bulk conductivity. The bulk energy band becomes completely independent in k_x as shown in Fig. 3.2, and then the Fermi surface becomes just two parallel lines at $k_z = \pm k_0$ along k_x direction. In this case, we can analytically solve the Boltzmann transport equation and derive the analytical expression of the bulk conductivity. Here we assume $L_y \gg \ell_B \gg d_0$, i.e., the slab is much thicker than the magnetic length, while the magnetic length is greater than the potential range. The result reads

$$\sigma_{zz}^\mathrm{bulk}(d_0) = \frac{e^2}{\hbar}\frac{1}{a}\frac{1}{w}\frac{1}{2\pi}\exp\left[\frac{\pi^2}{2}\frac{d_0^2}{a^2}\right], \tag{3.26}$$

where w characterizes the scattering strength and it is defined as $w = (n_{\rm i}u_0^2)/(\hbar^2 v^2 a)$. We see that the bulk conductivity exponentially increases with the increase of the potential range d_0. This is because the two branches at $k_z = \pm k_0$, traveling in the positive and negative directions, respectively, cannot be relaxed when the scattering potential is too smooth. This is exactly what was predicted by the early study [42, 43] and regarded an important consequence of the chiral anomaly. We also notice that the conductivity does not depend on the magnetic field B. Here the number of states (i.e., the Landau level degeneracy) increases as $\propto B$, but at the same time the relaxation time drops in inversely proportional to the number of states, resulting in the B-independent conductivity.

3.3 Conductivity of the surface-boundary system

The above property of the magnetoconductivity greatly changes in the presence of the surface. The deviation from the bulk is prominent particularly in the long-ranged scatterers, where the two bulk branches (the Landau levels with positive and negative velocities in z-direction) are not relaxed by the direct impurity scattering. In the presence of the surface, the significant relaxation takes place between them through hopping via the surface states, and that prevents the exponential increase of the conductivity.

We first present an analytic approximate solution of the Boltzmann equation [Eq. (3.25)] for the slab geometry in the long range limit: We completely neglect the direct scattering between the positive and negative bulk branches. We also assume that the distribution function $g_{\boldsymbol{k}}$ is non-zero only in the bulk states while it completely vanishes in the surface states. This is equivalent to the assumption that the momentum relaxation is much faster in the surface states than in the bulk states. This situation is actually achieved in the condition that the potential-range d_0 is much smaller than the magnetic length $\ell_{\rm B}$. We also impose the same condition as the bulk case, $L_y \gg \ell_{\rm B} \gg d_0$.

As a result, we obtain the scattering time $\tau_{\boldsymbol{k}}$ and $h_{\boldsymbol{k}}$

$$\tau(k_x) = \tau = \frac{2\pi\hbar^2 v}{n_{\rm i}u_0^2}\left(\ell_{\rm B}^2 + d_0^2\right), \tag{3.27}$$

$$h(k_x) = \mp v\left(1 + \frac{d_0^2}{\ell_{\rm B}^2}\right)\left(\ell_{\rm B}^2 k_x^2 - \frac{L_y^2}{4\ell_{\rm B}^2}\right), \tag{3.28}$$

where $\mp$ is for the positive- and the negative velocity branches ($k_z = \pm k_0$), respectively. The distribution function $g_{\boldsymbol{k}}$ is given by Eq. (3.12) and is proportional to $\tau_{\boldsymbol{k}} h_{\boldsymbol{k}}$.

The conductivity is derived as

$$\sigma_{zz}(d_0) = \frac{e^2}{\hbar}\frac{1}{a}\frac{1}{w}\frac{1}{6\pi}\left(1 + \frac{d_0^2}{\ell_{\rm B}^2}\right)^2 \frac{L_y^2}{\ell_{\rm B}^2}. \tag{3.29}$$

The biggest difference from the bulk case Eq. (3.26) is that the conductivity is just quartic in d_0 and does not exponentially increase in the long-range limit $d_0 \gg a$. Second, the conductivity is now dependent on the magnetic field $B(\propto 1/\ell_{\rm B}^2)$. In the low-field regime $\ell_{\rm B} \gg d_0$, it increases linearly to B, while it becomes super-linear in higher fields.

The above analytical formula well describes the qualitative feature of the exact solution. Now we numerically solve the Boltzmann equation [Eq. (3.25)], by discretizing the Fermi

surface into 400 k-points and the numerical iteration. We do not need any particular conditions here, and the obtained conductivity is valid (except for the numerical errors) for short-range and long-range cases as well.

Fig. 3.5 shows the conductivity as a function of d_0 at $N_y = 100$, with several different magnetic field $\phi = 0.003, 0.006, 0.009$. The inset shows the expanded plot in the small d_0 (short-range) region. The dotted curve is the analytic bulk conductivity [Eq. 3.26] and dashed lines are the analytic conductivity with the surface [Eq. 3.29]. We see that in the short-range region, the numerical result fit well to the bulk conductivity. In increasing d_0, however, the numerical solution does not follow the exponential increase of the bulk, but crosses over to the conductivity of the surface-bound system. We see that the analytic surface solution underestimates the conductivity in the large d_0 region, of which reason will be argued later.

Fig. 3.6 shows the magnetic-field dependence of the conductivity for several potential ranges $d_0 = 1.0, 2.0, 3.0$. Again, we see a similar cross-over between the bulk (dotted) and surface-bound (dashed) conductivities. In $d_0 = 1.0$, the numerical conductivity linearly rises in the low B-field regime like the surface-bound solution, while in the high-field it is bound by the bulk constant solution. In $d_0 = 2.0, 3.0$, the bulk conductivity is exponentially large (out of the range) and the numerical solution follows the super linear curve of the surface solution.

Fig. 3.7 shows the life time $\tau_{\boldsymbol{k}}$ and the renormalized distribution function $\tau_{\boldsymbol{k}} h_{\boldsymbol{k}}$. In the short-range case ($d_0 = 0$), the excessive carriers are distributed only in the bulk Landau level region, and it is almost flat within each of the positive and negative branches. This reflects that the two bulk branches are well coupled by the direct scatterings, and the situation is rather similar to the bulk. In increasing d_0, the distribution of the bulk states approaches the parabolic curve of the analytic surface solution [Eq. 3.28]. We also see that the distribution in the surface states is not zero anymore. This is due to the finite relaxation time in the surface states which was actually neglected in the analytic solution. The surface distribution becomes relatively more important in increasing d_0, and this accounts for the deviation of the numerical and analytical conductivity in Fig. 3.5 in the large d_0.

To conclude this chapter, we calculate the conductivity of the Weyl semimetal in $\mathbf{E} \parallel \mathbf{B}$ geometry with and without the system boundary. In the long range potential, the conductivity of the surface-bound system does not follow the exponential increase of the bulk system. There the surface states plays a critical role in the back scattering of the bulk carriers, otherwise the conductivity just diverges as previously assumed. We also find that the conductivities with and without the surface exhibit totally different properties in the magnetic field dependence, where the bulk conductivity is independent of B while the surface-bound system exhibits the B-linear behavior in the relatively low-field regime and super linear behavior in the higher field.

It should be noted that our calculation assumes the quantum limit where only the 0-th Landau level dominates the electron conduction. In a very weak magnetic field where the Landau level spacing is narrow, the other Landau levels start to contribute to the transport, and then the magnetoconductivity is expected to obey B^2 behavior in the semiclassical calculation. [46, 47, 52] The quantum limit is achieved when the Landau level spacing $\sqrt{2\hbar e B v^2}$ is much greater than the electronic energy broadening (inverse of the scattering life time) and the thermal broadening $k_{\mathrm{B}}T$.

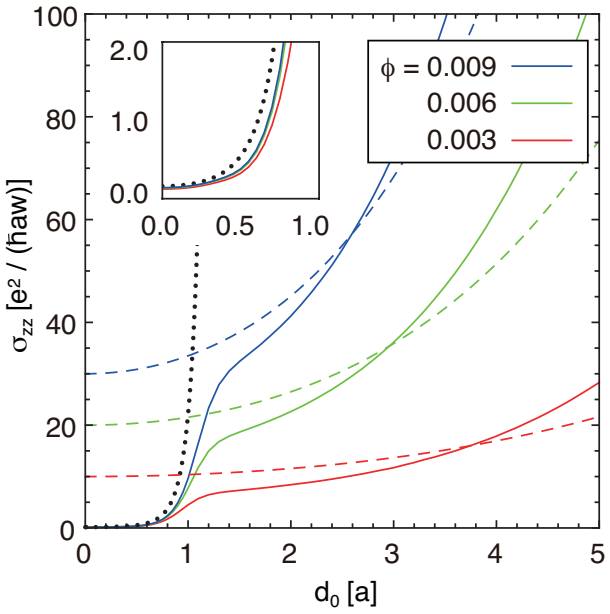

Figure 3.5: Conducticity as a function of d_0. We set $N_y = 100$, and $\phi = 0.003, 0.006, 0.009$.

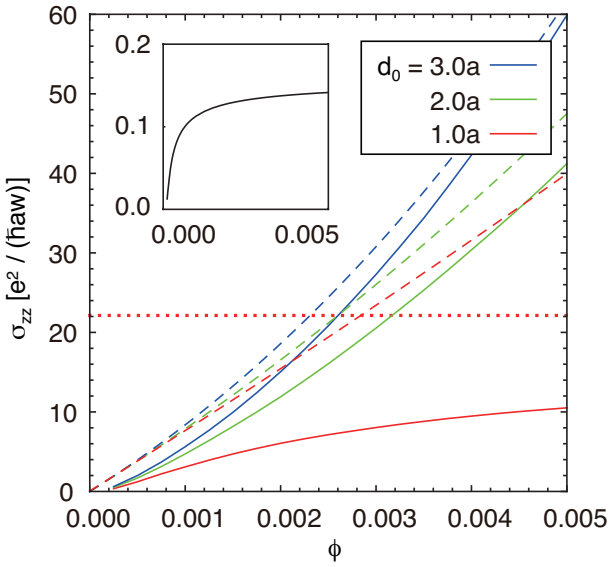

Figure 3.6: Conductivity as a function of ϕ. We set $N_y = 150$. $d_0 = 1.0a, 2.0a, 3.0a$. Inset is the short-range case ($d_0 = 0$).

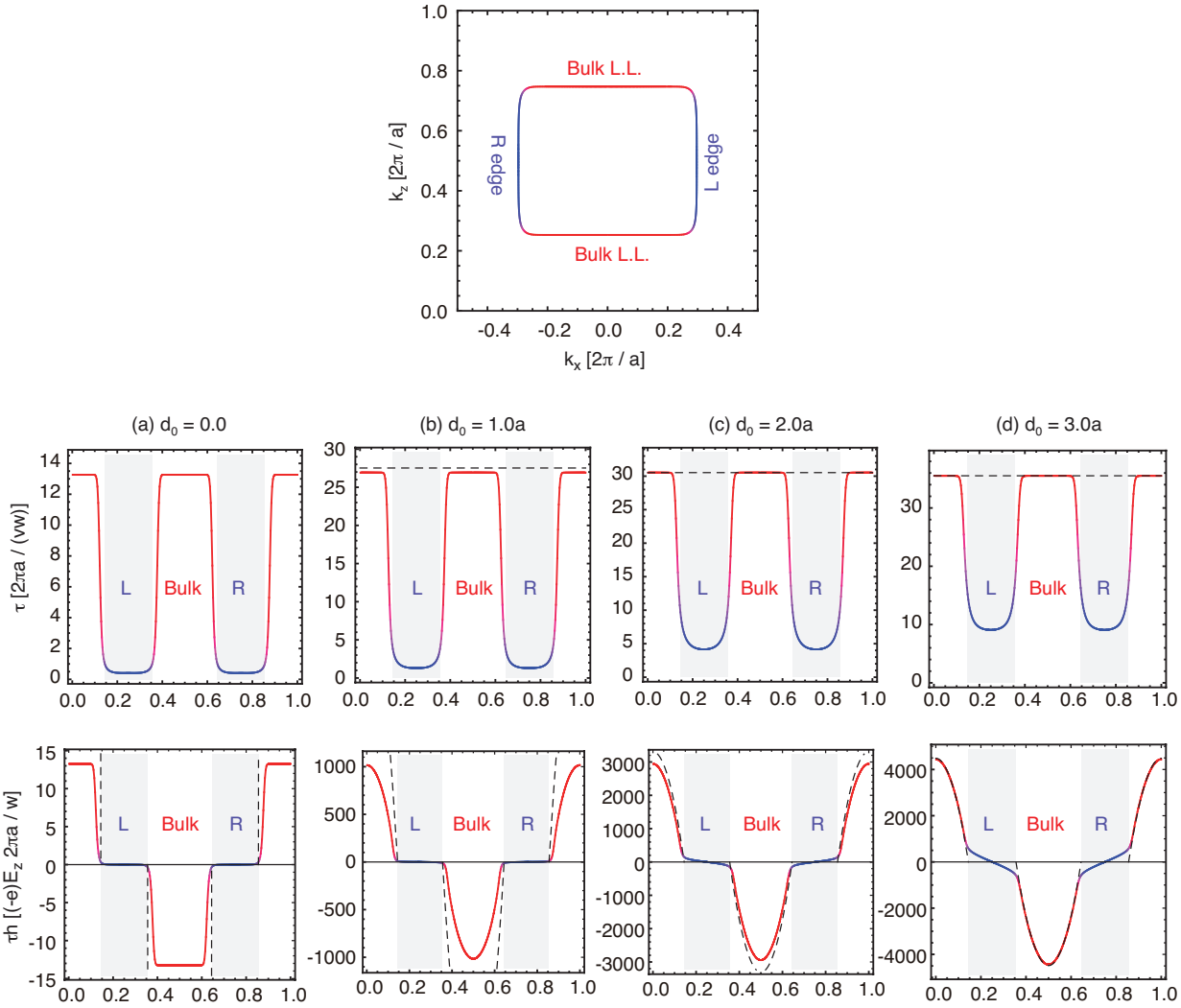

Figure 3.7: Relaxation time $\tau_{\boldsymbol{k}}$ (upper panels) and the renormalized distribution function $\tau_{\boldsymbol{k}} h_{\boldsymbol{k}}$ (lower) for several values of d_0. The dashed lines are analytically derived equations Eq. (3.27) and Eq. (3.28). The horizontal axis corresponds to the Fermi surface. Shaded region corresponding to the edge.

Chapter 4

Summary and Conclusion

In this thesis, we studied the quantum transport phenomena in the 3D Weyl electron systems. The 3D Weyl electron systems have the band-touching points (called the Weyl points) and the linear dispersion relation around the Weyl points. In the presence of the surface, we observe the surface energy bands which bridge the pair of the two Weyl points. There are many interesting transport phenomena which originate from the characteristic energy band structure. First, we focused on the quantum transport in the single-node 3D Weyl electrons, and the characteristic features near the Weyl point was unveiled. The detail is discussed in Chapter 2. Secondly, we discussed the magnetotransport in the Weyl semimetal, and we found that the surface states give the crucial contribution to the magnetotransport which is discussed in Chapter 3.

In Chapter 2, we studied the quantum transport in the single-node 3D Weyl electrons in the presence of the long-range disorder potentials. At the Weyl point, the Fermi surface becomes the point in the Brillouin zone and the density of states vanishes, so that we have to deal with the finite level broadening effect properly. We calculated the density of states and the conductivity within the self-consistent Born approximation (SCBA) which is one of the theoretical methods to treat the finite level broadening effect, and we found the characteristic features of the present system. The conductivity strongly depends on the type of the impurity potential and the disorder strength. In the Gaussian potential case, there is the critical disorder strength W_{c}, and the minimum conductivity (conductivity at the Weyl point) changes the behavior at the critical point. In the weak disorder regime, the minimum conductivity is zero, while in the strong disorder regime, the minimum conductivity has a finite value and abruptly rises with the increase of the disorder strength. In the finite Fermi energy, the conductivity is well approximated by the Boltzmann conductivity, but once the level broadening exceeds the Fermi energy, the Boltzmann theory fails and the conductivity increases with the increase of the disorder strength. In the Coulomb potential case, on the other hand, there is no critical behavior, and the minimum conductivity is determined solely by the impurity density n_{i}, and it scales in proportion to $n_{\mathrm{i}}^{1/3}$. The existence of the critical behavior is attributed to whether the system has a nonzero solution in the self-consistent equation for the self-energy, and we derived the analytical criteria for the existence of the critical behavior for general impurity potentials.

In Chapter 3, we studied the magnetotransport in $\mathbf{E} \parallel \mathbf{B}$ geometry. In general, one expect the physical properties of the system are dominated by the bulk contribution, and

the surface gives a minor correction. The existence of the surface states in the Weyl semimetal, however, drastically changes the behavior of the magnetoconductivity. We considered the Weyl semimetal which has two Weyl nodes. In the presence of the magnetic field, we have the Landau levels and there is the chiral 0th Landau level which has positive or negative velocity in each valley. In the presence of the surface, there are the surface bands which connect the two valleys, and the bulk states in each valley are seamlessly connected via the surface states. Using the Boltzmann transport theory, we calculated the magnetoconductivity in the presence of the long-range Gaussian scatterers. The magnetic and electric field are directed toward the same direction ($\mathbf{E} \parallel \mathbf{B}$ geometry). In the bulk system, the conductivity is exponentially large because of the exponentially small inter-valley scattering probability, and the conductivity diverges exponentially with the increase of the potential range. In the surface-boundary system, on the other hand, the conductivity exhibits significantly different behavior. The conductivity increases with the potential range, but it is not a exponential function but a quartic function of the potential range. This originates from the scattering process through the surface states which connect the bulk Landau level in each valley. In the bulk system, the conductivity is independent of the magnetic field B because of the cancellation of the dependence on B of the density of states ($\propto B$) and the relaxation time ($\propto B^{-1}$), while in the surface-boundary system, the conductivity depends on B in the super linear manner. This B dependence also originates from the scattering process through the surface states.

Acknowledgments

I would like to express my sincerest gratitude to Associate Professor Mikito Koshino for his continual guidance and encouragement throughout the course of the present work and his critical reading of the manuscript. I appreciate discussions with all the members of the condensed matter physics theory group.

Publication list

Publications related to the present PhD thesis

1. Y. Ominato and M. Koshino, Phys. Rev. B **89**, 054202 (2014).
"Quantum transport in a three-dimensional Weyl electron system"

2. Y. Ominato and M. Koshino, Phys. Rev. B **91**, 035202 (2015).
"Quantum transport in three-dimensional Weyl electron system in the presence of charged impurity scattering"

3. Y. Ominato and M. Koshino, arXiv:1512.08223 (2015).
"Magnetotransport in the Weyl semimetal in the quantum limit - the role of the topological surface states"

Other publications

4. Y. Ominato and M. Koshino, Phys. Rev. B **85**, 165454 (2012).
"Orbital magnetic susceptibility of finite-sized graphene"

5. Y. Ominato and M. Koshino, Phys. Rev. B **87**, 115433 (2013).
"Orbital magnetism of graphene flakes"

6. Y. Ominato and M. Koshino, Solid State Commun. **175-176**, 51 (2013).
"Orbital magnetism of graphene nanostructures"

Bibliography

[1] AA Burkov and Leon Balents. Weyl semimetal in a topological insulator multilayer. *Phys. Rev. Lett.*, 107(12):127205, 2011.

[2] AA Burkov, MD Hook, and Leon Balents. Topological nodal semimetals. *Phys. Rev. B*, 84(23):235126, 2011.

[3] Xiangang Wan, Ari M Turner, Ashvin Vishwanath, and Sergey Y Savrasov. Topological semimetal and fermi-arc surface states in the electronic structure of pyrochlore iridates. *Phys. Rev. B*, 83(20):205101, 2011.

[4] Kai-Yu Yang, Yuan-Ming Lu, and Ying Ran. Quantum hall effects in a weyl semimetal: Possible application in pyrochlore iridates. *Physical Review B*, 84(7):075129, 2011.

[5] Steve M Young, Saad Zaheer, Jeffrey CY Teo, Charles L Kane, Eugene J Mele, and Andrew M Rappe. Dirac semimetal in three dimensions. *Phys. Rev. Lett.*, 108(14):140405, 2012.

[6] Zhijun Wang, Yan Sun, Xing-Qiu Chen, Cesare Franchini, Gang Xu, Hongming Weng, Xi Dai, and Zhong Fang. Dirac semimetal and topological phase transitions in a_ {3} bi (a= na, k, rb). *Phys. Rev. B*, 85(19):195320, 2012.

[7] Bahadur Singh, Ashutosh Sharma, H Lin, MZ Hasan, R Prasad, and A Bansil. Topological electronic structure and weyl semimetal in the tlbise_ {2} class of semiconductors. *Phys. Rev. B*, 86(11):115208, 2012.

[8] JC Smith, S Banerjee, V Pardo, and WE Pickett. Dirac point degenerate with massive bands at a topological quantum critical point. *Phys. Rev. Lett.*, 106(5):056401, 2011.

[9] Chao-Xing Liu, Peng Ye, and Xiao-Liang Qi. Chiral gauge field and axial anomaly in a weyl semimetal. *Phys. Rev. B*, 87(23):235306, 2013.

[10] William Witczak-Krempa and Yong Baek Kim. Topological and magnetic phases of interacting electrons in the pyrochlore iridates. *Phys. Rev. B*, 85(4):045124, 2012.

[11] Gang Xu, Hongming Weng, Zhijun Wang, Xi Dai, and Zhong Fang. Chern semimetal and the quantized anomalous hall effect in hgcr_ {2} se_ {4}. *Phys. Rev. Lett.*, 107(18):186806, 2011.

[12] Gil Young Cho. Possible topological phases of bulk magnetically doped bi2se3: turning a topological band insulator into the weyl semimetal. *arXiv:1110.1939*, 2012.

[13] Gábor B Halász and Leon Balents. Time-reversal invariant realization of the weyl semimetal phase. *Phys. Rev. B*, 85(3):035103, 2012.

[14] Shuichi Murakami. Phase transition between the quantum spin hall and insulator phases in 3d: emergence of a topological gapless phase. *New J. Phys.*, 9(9):356, 2007.

[15] Sergey Borisenko, Quinn Gibson, Danil Evtushinsky, Volodymyr Zabolotnyy, Bernd Büchner, and Robert J. Cava. Experimental realization of a three-dimensional dirac semimetal. *Phys. Rev. Lett.*, 113:027603, Jul 2014.

[16] Madhab Neupane, Su-Yang Xu, Raman Sankar, Nasser Alidoust, Guang Bian, Chang Liu, Ilya Belopolski, Tay-Rong Chang, Horng-Tay Jeng, Hsin Lin, et al. Observation of a three-dimensional topological dirac semimetal phase in high-mobility cd3as2. *Nature communications*, 5:3786, 2014.

[17] ZK Liu, B Zhou, Y Zhang, ZJ Wang, HM Weng, D Prabhakaran, S-K Mo, ZX Shen, Z Fang, X Dai, et al. Discovery of a three-dimensional topological dirac semimetal, na3bi. *Science*, 343(6173):864–867, 2014.

[18] Su-Yang Xu, Ilya Belopolski, Nasser Alidoust, Madhab Neupane, Guang Bian, Chenglong Zhang, Raman Sankar, Guoqing Chang, Zhujun Yuan, Chi-Cheng Lee, et al. Discovery of a weyl fermion semimetal and topological fermi arcs. *Science*, 349(6248):613–617, 2015.

[19] B. Q. Lv, H. M. Weng, B. B. Fu, X. P. Wang, H. Miao, J. Ma, P. Richard, X. C. Huang, L. X. Zhao, G. F. Chen, Z. Fang, X. Dai, T. Qian, and H. Ding. Experimental discovery of weyl semimetal taas. *Phys. Rev. X*, 5:031013, Jul 2015.

[20] Horst Borrmann, Yuri Grin, Claudia Felser, and Binghai Yan. Extremely large magnetoresistance and ultrahigh mobility in the topological weyl semimetal candidate nbp. 2015.

[21] Su-Yang Xu, Ilya Belopolski, Daniel S Sanchez, Chenglong Zhang, Guoqing Chang, Cheng Guo, Guang Bian, Zhujun Yuan, Hong Lu, Tay-Rong Chang, et al. Experimental discovery of a topological weyl semimetal state in tap. *Science Advances*, 1(10):e1501092, 2015.

[22] Eduardo Fradkin. Critical behavior of disordered degenerate semiconductors. ii. spectrum and transport properties in mean-field theory. *Phys. Rev. B*, 33(5):3263, 1986.

[23] Andreas WW Ludwig, Matthew PA Fisher, R Shankar, and G Grinstein. Integer quantum hall transition: An alternative approach and exact results. *Phys. Rev. B*, 50(11):7526, 1994.

[24] Nguyen Hong Shon and Tsuneya Ando. Quantum transport in two-dimensional graphite system. *J. Phys. Soc. Jpn.*, 67(7):2421–2429, 1998.

[25] K Ziegler. Delocalization of 2d dirac fermions: The role of a broken supersymmetry. *Physical Rev. Lett.*, 80(14):3113, 1998.

[26] J Tworzydło, Björn Trauzettel, M Titov, Adam Rycerz, and Carlo WJ Beenakker. Sub-poissonian shot noise in graphene. *Physical Rev. Lett.*, 96(24):246802, 2006.

[27] MI Katsnelson. Zitterbewegung, chirality, and minimal conductivity in graphene. *Eur. Phys. J. B*, 51(2):157–160, 2006.

[28] Tsuneya Ando. Screening effect and impurity scattering in monolayer graphene. *Journal of the Physical Society of Japan*, 75(7):074716, 2006.

[29] Kentaro Nomura and AH MacDonald. Quantum transport of massless dirac fermions. *Physical review letters*, 98(7):076602, 2007.

[30] Masaki Noro, Mikito Koshino, and Tsuneya Ando. Theory of transport in graphene with long-range scatterers. *J. Phys. Soc. Jpn.*, 79(9):094713, 2010.

[31] KSA Novoselov, Ak K Geim, SVb Morozov, Da Jiang, MI Katsnelson IV Grigorieva, SV Dubonos, and AA Firsov. Two-dimensional gas of massless dirac fermions in graphene. *Nature*, 438(7065):197–200, 2005.

[32] Y-W Tan, Y Zhang, K Bolotin, Y Zhao, S Adam, EH Hwang, S Das Sarma, HL Stormer, and Ph Kim. Measurement of scattering rate and minimum conductivity in graphene. *Physical Review Letters*, 99(24):246803, 2007.

[33] J-H Chen, C Jang, S Adam, MS Fuhrer, ED Williams, and Masa Ishigami. Charged-impurity scattering in graphene. *Nature Physics*, 4(5):377–381, 2008.

[34] Ryuichi Shindou and Shuichi Murakami. Effects of disorder in three-dimensional z 2 quantum spin hall systems. *Physical Review B*, 79(4):045321, 2009.

[35] Eduardo Fradkin. Critical behavior of disordered degenerate semiconductors. i. models, symmetries, and formalism. *Phys. Rev. B*, 33(5):3257, 1986.

[36] Pavan Hosur, SA Parameswaran, and Ashvin Vishwanath. Charge transport in weyl semimetals. *Phys. Rev. Lett.*, 108(4):046602, 2012.

[37] Koji Kobayashi, Tomi Ohtsuki, Ken-Ichiro Imura, and Igor F. Herbut. Density of states scaling at the semimetal to metal transition in three dimensional topological insulators. *Phys. Rev. Lett.*, 112:016402, 2014.

[38] Rahul Nandkishore, David A Huse, and SL Sondhi. Rare region effects dominate weakly disordered three-dimensional dirac points. *Physical Review B*, 89(24):245110, 2014.

[39] Rudro R Biswas and Shinsei Ryu. Diffusive transport in weyl semimetals. *Physical Review B*, 89(1):014205, 2014.

[40] Yuya Ominato and Mikito Koshino. Quantum transport in a three-dimensional weyl electron system. *Physical Review B*, 89(5):054202, 2014.

[41] Yuya Ominato and Mikito Koshino. Quantum transport in three-dimensional weyl electron system in the presence of charged impurity scattering. *Physical Review B*, 91(3):035202, 2015.

[42] Holger Bech Nielsen and Masao Ninomiya. Absence of neutrinos on a lattice:(i). proof by homotopy theory. *Nucl. Phys. B*, 185(1):20–40, 1981.

[43] Holger Bech Nielsen and Masao Ninomiya. Absence of neutrinos on a lattice:(ii). intuitive topological proof. *Nucl. Phys. B*, 193(1):173–194, 1981.

[44] Holger Bech Nielsen and Masao Ninomiya. The adler-bell-jackiw anomaly and weyl fermions in a crystal. *Physics Letters B*, 130(6):389–396, 1983.

[45] Vivek Aji. Adler-bell-jackiw anomaly in weyl semimetals: Application to pyrochlore iridates. *Physical Review B*, 85(24):241101, 2012.

[46] D. T. Son and B. Z. Spivak. Chiral anomaly and classical negative magnetoresistance of weyl metals. *Phys. Rev. B*, 88:104412, Sep 2013.

[47] AA Burkov. Chiral anomaly and diffusive magnetotransport in weyl metals. *Physical review letters*, 113(24):247203, 2014.

[48] EV Gorbar, VA Miransky, and IA Shovkovy. Chiral anomaly, dimensional reduction, and magnetoresistivity of weyl and dirac semimetals. *Physical Review B*, 89(8):085126, 2014.

[49] Dmitri E Kharzeev. The chiral magnetic effect and anomaly-induced transport. *Progress in Particle and Nuclear Physics*, 75:133–151, 2014.

[50] Ming-Che Chang and Min-Fong Yang. Chiral magnetic effect in a two-band lattice model of weyl semimetal. *Phys. Rev. B*, 91:115203, Mar 2015.

[51] Hai-Zhou Lu, Song-Bo Zhang, and Shun-Qing Shen. High-field magnetoconductivity of topological semimetals with short-range potential. *Physical Review B*, 92(4):045203, 2015.

[52] AA Burkov. Negative longitudinal magnetoresistance in dirac and weyl metals. *Phys. Rev. B*, 91:245157, 2015.

[53] Heon-Jung Kim, Ki-Seok Kim, J-F Wang, M Sasaki, N Satoh, A Ohnishi, M Kitaura, M Yang, and L Li. Dirac versus weyl fermions in topological insulators: Adler-bell-jackiw anomaly in transport phenomena. *Physical review letters*, 111(24):246603, 2013.

[54] Hui Li, Hongtao He, Hai-Zhou Lu, Huachen Zhang, Hongchao Liu, Rong Ma, Zhiyong Fan, Shun-Qing Shen, and Jiannong Wang. Negative magnetoresistance in dirac semimetal cd3as2. *arXiv preprint arXiv:1507.06470*, 2015.

[55] Xiaojun Yang, Yupeng Liu, Zhen Wang, Yi Zheng, and Zhu-an Xu. Chiral anomaly induced negative magnetoresistance in topological weyl semimetal nbas. *arXiv preprint arXiv:1506.03190*, 2015.

[56] Cheng Zhang, Enze Zhang, Yanwen Liu, Zhi-Gang Chen, Sihang Liang, Junzhi Cao, Xiang Yuan, Lei Tang, Qian Li, Teng Gu, et al. Detection of chiral anomaly and valley transport in dirac semimetals. *arXiv preprint arXiv:1504.07698*, 2015.

[57] Cai-Zhen Li, Li-Xian Wang, Haiwen Liu, Jian Wang, Zhi-Min Liao, and Da-Peng Yu. Giant negative magnetoresistance induced by the chiral anomaly in individual cd3as2 nanowires. *arXiv preprint arXiv:1504.07398*, 2015.

[58] Chenglong Zhang, Su-Yang Xu, Ilya Belopolski, Zhujun Yuan, Ziquan Lin, Bingbing Tong, Nasser Alidoust, Chi-Cheng Lee, Shin-Ming Huang, Hsin Lin, et al. Observation of the adler-bell-jackiw chiral anomaly in a weyl semimetal. *arXiv preprint arXiv:1503.02630*, 2015.

[59] Xiaochun Huang, Lingxiao Zhao, Yujia Long, Peipei Wang, Dong Chen, Zhanhai Yang, Hui Liang, Mianqi Xue, Hongming Weng, Zhong Fang, Xi Dai, and Genfu Chen. Observation of the chiral-anomaly-induced negative magnetoresistance in 3d weyl semimetal taas. *Phys. Rev. X*, 5:031023, Aug 2015.

[60] Jun Xiong, Satya K Kushwaha, Tian Liang, Jason W Krizan, Max Hirschberger, Wudi Wang, RJ Cava, and NP Ong. Evidence for the chiral anomaly in the dirac semimetal na3bi. *Science*, 350(6259):413–416, 2015.

[61] Sangjun Jeon, Brian B Zhou, Andras Gyenis, Benjamin E Feldman, Itamar Kimchi, Andrew C Potter, Quinn D Gibson, Robert J Cava, Ashvin Vishwanath, and Ali Yazdani. Landau quantization and quasiparticle interference in the three-dimensional dirac semimetal cd3as2. *Nature Materials*, 13:851, 2014.

[62] J-P Jay-Gerin, MJ Aubin, and LG Caron. The electron mobility and the static dielectric constant of cd¡ sub¿ 3¡/sub¿ as¡ sub¿ 2¡/sub¿ at 4.2 k. *Solid State Communications*, 21(8):771–774, 1977.

[63] PM Ostrovsky, IV Gornyi, and AD Mirlin. Electron transport in disordered graphene. *Physical Review B*, 74(23):235443, 2006.

[64] Björn Sbierski, Gregor Pohl, Emil J. Bergholtz, and Piet W. Brouwer. Quantum transport of disordered weyl semimetals at the nodal point. *Phys. Rev. Lett.*, 113:026602, Jul 2014.